

1 **Title: A human monoclonal antibody potently pan-neutralizes SARS-CoV-2**
2 **VOCs by targeting RBD invariant sites**

3
4 **Authors:** Xiaofei Wang^{1,2,3,†}, Ao Hu^{1,†}, Xiangyu Chen^{4,5,†}, Yixin Zhang^{1,†}, Fei Yu^{1,6,†},
5 Shuai Yue⁷, Arong Li^{2,3}, Junsong Zhang^{1,6}, Zhiwei Pan⁷, Yang Yang⁴, Yao Lin⁷,
6 Leiqiong Gao⁷, Jing Zhou⁷, Jing Zhao⁸, Fang Li^{9,10}, Yaling Shi⁹, Feng Huang^{1,6},
7 Xiaofan Yang¹, Yi Peng¹, Luoyang Tu¹, Huan Zhang¹¹, Huanying Zheng¹¹, Jun He¹²,
8 Hui Zhang¹, Lifan Xu⁷, Qizhao Huang⁴, Yongqun Zhu^{2,3,*}, Kai Deng^{1,*}, Lilin Ye^{7,*}

9
10 **Affiliations:**

11 ¹Institute of Human Virology, Key Laboratory of Tropical Disease Control of Ministry
12 of Education, Zhongshan School of Medicine, Sun Yat-sen University, Guangzhou,
13 Guangdong, China.

14 ²Department of Gastroenterology of the Second Affiliated Hospital School of
15 Medicine, and Life Sciences Institute, Zhejiang University, Hangzhou, Zhejiang,
16 China.

17 ³The MOE Key Laboratory for Biosystems Homeostasis & Protection and Zhejiang
18 Provincial Key Laboratory of Cancer Molecular Cell Biology, Life Sciences Institute,
19 Zhejiang University, Hangzhou, Zhejiang, China.

20 ⁴School of Laboratory Medicine and Biotechnology, Southern Medical University,
21 Guangzhou, Guangdong, China.

22 ⁵Institute of Cancer, Xinqiao Hospital, Third Military Medical University, Chongqing
23 400038, China.

24 ⁶Medical Research Center, Guangdong Provincial People's Hospital, Guangdong
25 Academy of Medical Sciences, Guangzhou, Guangdong, China.

26 ⁷Institute of Immunology, PLA, Third Military Medical University, Chongqing,
27 China.

28 ⁸Biomedical Analysis Center, Third Military Medical University, Chongqing, China.

29 ⁹Guangzhou Eighth People's Hospital, Guangzhou Medical University, Guangzhou,
30 Guangdong, China.

31 ¹⁰Guangzhou Women and Children Medical Center, Guangzhou Medical University,
32 Guangzhou, Guangdong, China.

33 ¹¹Guangdong Provincial Center for Disease Control and Prevention, Guangzhou,
34 Guangdong, China.

35 ¹²Center for Cell Lineage and Development, Guangzhou Institutes of Biomedicine
36 and Health, Chinese Academy of Sciences, Guangzhou, Guangdong, China.

37 †These authors contributed equally to this work.

38 *Correspondence: Yongqun Zhu (zhuyongqun@zju.edu.cn), Kai Deng
39 (dengkai6@mail.sysu.edu.cn) and Lilin Ye (yelilinlcmv@tmmu.edu.cn).

40

41 **Abstract**

42 The severe acute respiratory syndrome coronavirus 2 (SARS-CoV-2) has caused a
43 global pandemic of novel corona virus disease (COVID-19). The neutralizing
44 monoclonal antibodies (mAbs) targeting the receptor binding domain (RBD) of
45 SARS-CoV-2 are among the most promising strategies to prevent and treat
46 COVID-19. However, SARS-CoV-2 variants of concern (VOCs) profoundly reduced
47 the efficacies of most of mAbs and vaccines approved for clinical use. Herein, we
48 demonstrated mAb 35B5 efficiently neutralizes both wild-type (WT) SARS-CoV-2
49 and VOCs, including B.1.617.2 (delta) variant, *in vitro* and *in vivo*. Cryo-electron
50 microscopy (cryo-EM) revealed that 35B5 neutralizes SARS-CoV-2 by targeting a
51 unique epitope that avoids the prevailing mutation sites on RBD identified in
52 circulating VOCs, providing the molecular basis for its pan-neutralizing efficacy. The
53 35B5-binding epitope could also be exploited for the rational design of a universal
54 SARS-CoV-2 vaccine.
55

56 **Introduction**

57 As of November 23rd, 2021, the novel coronavirus SARS-CoV-2 has resulted in more
58 than 256.48 million cases and 5.14 million fatalities¹. Though an unprecedentedly
59 large number of vaccines and neutralizing mAbs have been developed to contain
60 COVID-19 in the past year, a major concern is the emergence of more transmissible
61 and/or more immune evasive SARS-CoV-2 VOCs, which are antigenically distinct
62 and become dominant in the COVID-19 prevalence over time^{2,3}. Indeed, the D614G
63 variant became prevalent in the early phase of the pandemic and was associated with
64 higher transmission rate⁴. As the thriving pandemic continued, a rapid accumulation
65 of mutations was observed in SARS-CoV-2 and thus seeded the simultaneous
66 appearance of a plethora of VOCs, which include but not limited to B.1.1.7 (UK;
67 alpha variant)⁵, B.1.351 (SA; beta variant)⁶, P.1 (Brazil; gamma variant)⁷, B.1.617.2
68 (India; delta variant)⁸ and newly identified B.1.1.529 (SA; omicron variant)⁹.

69 In the RBD of SARS-CoV-2 spike protein, B.1.1.7 harbors a N501Y mutation
70 and thus acquires enhanced binding of RBD to the human receptor ACE2^{3,5}. Along
71 with the N501Y mutation, B.1.351 and P.1 develop additional K417N/T and E484K
72 mutations^{6,7}. Meanwhile, B.1.617.2 carries E484Q/L452R mutations⁸. These
73 mutations contribute to the immune escape of SARS-CoV-2 VOCs against many
74 mAbs^{3,10,11,12}, including those already approved for clinical use (casirivimab,
75 bamlanivimab, regdanvimab). These mutant VOCs also undermine humoral immune
76 response elicited by the WT SARS-CoV-2 infection or vaccines targeting WT

77 SARS-CoV-2 protein sequence^{11, 12, 13, 14, 15, 16}. Thus, highly potent and broadly
78 neutralizing mAbs targeting multiple SARS-CoV-2 VOCs are urgently needed for
79 emergency use and elucidating the underlying neutralizing mechanisms of broadly
80 neutralizing mAbs will also provide important insights into the rational design of
81 universal SARS-CoV-2 vaccines.

82

83 **Results**

84 **Isolation and characteristics of mAbs 35B5 and 32C7**

85 To discover potent broadly neutralizing mAbs against circulating SARS-CoV-2 VOCs,
86 we adapted a pipeline to rapidly isolate and characterize mAbs (Supplementary fig.
87 1a). Given the vigorous SARS-CoV-2-specific memory B cell response in individuals
88 recovering from severe COVID-19 illness^{17, 18}, cryopreserved PBMCs from these
89 convalescent patients with WT SARS-CoV-2 infection were stained for memory B
90 cell markers (CD19, CD20 and IgG) and avidin-tagged biotinylated SARS-CoV-2
91 RBD antigen bait. As expected, we found SARS-CoV-2 RBD-specific memory B
92 cells only enriched in PBMCs of convalescent COVID-19 patients, but not healthy
93 donors (Supplementary fig. 1b). Each individual of SARS-CoV-2 RBD-specific
94 memory B cells was further sorted to clone heavy and light chain pairs for mAb
95 production. Two mAbs potentially with superior neutralization activity, one
96 VH3-9/VK2-28 mAb named as 35B5, characterized by a heavy chain CDR3 region of
97 23 residues and a light chain CDR3 region of 9 residues and another VH3-30/VK4-1

98 mAb named as 32C7, featured by heavy chain CDR3 of 16 residues and light chain
99 CDR3 of 9 residues (Supplementary fig. 1c, d), were cloned, expressed and analyzed.

100 Real-time association and dissociation of 35B5 and 32C7 binding to the RBD of
101 SARS-CoV-2 virus were monitored using the surface plasmon resonance (SPR)-based
102 optical assay. We found that 35B5 and 32C7 exhibited different binding affinity in
103 binding to SARS-CoV-2 RBD. Notably, 35B5 exhibited fast-on/slow-off kinetics with
104 an equilibrium dissociation constant (K_D) of 2.19×10^{-12} M and its binding affinity for
105 SARS-CoV-2 RBD is close to the detection limit at sub-nM level (Fig. 1a); whereas
106 32C7 showed slow-on/fast-off kinetics with a K_D of 1.09×10^{-8} M (Fig. 1b).
107 Consistently, these binding modes were further evidenced by enzyme-linked
108 immunosorbent assay (ELISA) for SARS-CoV-2 RBD, with a EC_{50} value of 0.0183
109 $\mu\text{g/ml}$ for 35B5 and a EC_{50} value of 0.1038 $\mu\text{g/ml}$ for 32C7 (Supplementary fig. 1e).

110

111 **Potent neutralization capacity of mAbs 35B5 to SARS-CoV-2 virus *in vitro* and *in*** 112 ***vivo***

113 We next investigated the neutralizing capacity of 35B5 and 32C7 against authentic
114 WT SARS-CoV-2 infection in Vero E6 cells. Remarkably, we found that both 35B5
115 and 32C7 neutralized authentic SARS-CoV-2 virus in the low picomolar range, with
116 observed IC_{50} values of 1.55 ng/ml for 35B5 (Fig. 1c) and 8.60 ng/ml for 32C7 (Fig.
117 1d). We further assessed *in vivo* protection efficacy of 35B5 and 32C7 in the human
118 ACE2 (hACE2)-expressing transgenic mouse model (ICR background) that is

119 sensitized to SARS-CoV-2 infection¹⁹. The hACE2-humanized mice were treated
120 intraperitoneally with a single dose of 35B5 or 32C7 with 20 mg/kg at 6 hours after
121 intranasal infection with 4×10^4 PFU of SARS-CoV-2. As control, infected mice of
122 mock group were administrated with an equal volume of PBS (Fig. 1e). At day 5
123 post-infection, the viral loads in the lungs of the mock group surged to $\sim 10^4$ RNA
124 copies/ml (Fig. 1f). By contrast, 35B5 and 32C7 treatment remarkably reduced the
125 viral titers, with $\sim 10^2$ RNA copies/ml resulting 100-fold reduction and $\sim 10^3$ RNA
126 copies/ml resulting 10-fold reduction, respectively (Fig. 1f). In addition, we also
127 determined whether 35B5 and 32C7 treatment ameliorated the pathological lung
128 damage in the hACE2 mice infected with SARS-CoV-2. The transcripts of cytokines
129 and chemokines (e.g., *Ccl2*, *Cxcl1*, *Il1b*, *Il6* and *Tnf*), indicative of tissue
130 inflammation, were greatly reduced in both 35B5- and 32C7-treated groups when
131 compared to those observed in the mock group (Fig. 1g). Parallely, the SARS-CoV-2
132 virus caused interstitial pneumonia characterized by inflammatory cell infiltration,
133 alveolar septal thickening and distinctive vascular system injury in the mock group,
134 but not in 35B5 or 32C7 treatment groups; additionally, less pronounced lesions of
135 alveolar epithelial cells or focal hemorrhage were observed in the lung sections from
136 mice that received 35B5 or 32C7 treatment than in those from mice of mock group
137 (Fig. 1h). Thus, these results together indicate the potential therapeutic role for these
138 two mAbs, in particular 35B5, in treating COVID-19.

139

140 **35B5 exhibits ultrapotent and broad neutralization activity to SARS-CoV-2**

141 **VOCs *in vitro* and *in vivo***

142 We then sought to determine the neutralizing capacity of 35B5 and 32C7 mAbs
143 against SARS-CoV-2 variants. Neutralizing activity of these two mAbs was assessed
144 against authentic SARS-CoV-2 viruses, including WT, D614G, B.1.351 and B.1.617.2
145 strains. It turned out 35B5 preserved highly potent neutralizing capacity against the
146 D614G variant ($IC_{50}=7.29$ ng/ml), the B.1.351 variant ($IC_{50}=13.04$ ng/ml) and the
147 B.1.617.2 variant ($IC_{50}=5.63$ ng/ml) (Fig. 2a); however, neutralizing capacity of 32C7
148 against these two variants was severely blunted, with IC_{50} values of 127.60 ng/ml for
149 the D614G variant, 1420.00 ng/ml for the B.1.351 variant and 3442.00 ng/ml for the
150 B.1.617.2 variant (Fig. 2b). In parallel, we also explored the neutralization of
151 authentic virus by 35B5 and 32C7 in a focus forming assay (FFA). Consistently, we
152 found that 35B5 showed potent neutralizing capacity against the WT SARS-CoV-2,
153 the D614G variant, the B.1.351 variant as well as the B.1.617.2 variant (Fig. 2c);
154 whereas 32C7 exhibited a clear reduction in neutralization against the D614G variant,
155 the B.1.351 variant and the B.1.617.2 variant (Fig. 2d). Given the highly broad
156 neutralization activities of 35B5 *in vitro*, we next assessed the *in vivo* protection
157 efficacy of 35B5 against the D614G variant, the B.1.351 variant and the B.1.617.2
158 variant. To this end, a different strain of hACE2-humanized mice (C57BL/6
159 background)²⁰ were infected with 4×10^4 PFU of SARS-CoV-2 D614G or B.1.351 or
160 B.1.617.2 and then treated with a single dose of 35B5 with 30 mg/kg or PBS at 4

161 hours after infection. Viral loads in the lungs of all infected mice were measured at
162 day 5 post-infection (Fig. 2e). Indeed, we found that 35B5 treatment resulted in a
163 ~10-fold, ~100-fold and ~100-fold reduction of viral titers in the lungs of mice
164 infected with D614G, B.1.351 and B.1.617.2, respectively (Fig. 2f). Moreover, tissue
165 inflammation and interstitial pneumonia caused by SARS-CoV-2
166 D614G/B.1.351/B.1.617.2 infection were largely ameliorated in 35B5-treated groups
167 compared to that in mock groups (Fig. 2g-j). Together, these results suggest that 35B5
168 potently neutralizes a variety of SARS-CoV-2 variants as a broadly neutralizing mAb.
169

170 **Complex structure of mAb 35B5 with the spike protein**

171 To investigate the structural basis of the superior and broad neutralizing activity of
172 35B5 against the SARS-CoV-2 variants, we employed cryo-EM approaches to
173 determine the complex structure of the Fab region of 35B5 with the spike protein of
174 SARS-CoV-2. Incubation of 35B5 Fab with the ectodomain of the spike protein
175 S-2P²¹, a stabilized spike mutant, severely caused the dissociation of the trimer and
176 disrupted its structure quickly *in vitro* (Supplementary Fig. 2). 35B5 Fab even
177 disrupted the ectodomain trimer structure of the spike S-HexaPro protein (S-6P)²², a
178 more stable spike variant containing four additional proline substitutions (F817P,
179 A892P, A899P and A942P) from S-2P (Supplementary Fig. 2), suggesting that 35B5
180 harbors the potent dissociation activity toward the spike protein. Nonetheless, a few of
181 the S-6P particles were still found to maintain the triangular architecture^{22, 23} after

182 35B5 Fab treatment for 3 min, which thereby allowed us to carry out cryo-EM
183 analyses of the 35B5 Fab-S-6P complex. We successfully determined the structures of
184 the 35B5 Fab-S-6P complex in three conformational states to the resolutions of 3.7 Å,
185 3.4 Å and 3.6 Å, respectively (Supplementary Fig. 3 and Supplementary Table 1).

186 In the 35B5 Fab-S-6P complex structure of State 1, two RBD domains of the S-6P
187 trimer are in the standard “up” conformations²¹ and are bound by 35B5 Fabs (Fig. 3a).
188 The other RBD domain is in the “down” conformation²¹ as that was found in the
189 Fab-free spike trimers. In the 35B5 Fab-S-6P complex structure of State 2, each of the
190 three RBD domains was in the “up” conformation and bound by a 35B5 Fab (Fig. 3a).
191 In the 35B5 Fab-S-6P complex structure of State 3, although all the three RBD
192 domains were bound by 35B5 Fab, only one RBD domain maintained the “up”
193 conformation. The other two RBD domains were in unprecedented conformations,
194 which we for the first time named as “releasing” conformations (Fig. 3a). Compared
195 to the “up” RBDs, the two “releasing” RBD domains move out by 6.4 Å and 23.0 Å,
196 respectively (Fig. 4f). The two “releasing” RBD domains generated large gaps with
197 the adjacent NTD domains in the S-6P trimers (Fig. 3a), suggesting that the spike
198 protein is undergoing structural dissociation.

199

200 **35B5 targets a unique epitope for pan-neutralizing activity**

201 The interactions of 35B5 Fab with the “up” RBDs are identical to those of 35B5 Fab
202 with the “releasing” RBDs in the three states of the 35B5 Fab-S-6P complex. The

203 interface covers a largely buried area of $\sim 1029 \text{ \AA}^2$ (Fig. 3b, c). The epitope in RBD
204 for 35B5 is composed of 30 interacting residues including R346, F347, N354, R466,
205 A352, K444, Y449, N450, R466, I468, T470, N481, and F490, which form extensive
206 hydrophilic interactions with 35B5 Fab in the structure (Fig. 3b-f). The corresponding
207 paratope in 35B5 Fab consists of two heavy chain complementarity determining
208 regions (CDRH2 and CDRH3) and the heavy chain frameworks (FRH1 and FRH3).
209 The epitope of 35B5 on RBD is distinct from those of the previously identified 4
210 classes of neutralizing antibodies to RBD²⁴. The 35B5 Fab-binding surface on RBD is
211 located at the site opposite to the receptor ACE2-binding surface^{24, 25, 26, 27}, which is
212 targeted by the class 1 antibodies, suggesting that 35B5 doesn't directly block the
213 receptor recognition for neutralization. Although the epitope of 35B5 Fab involves
214 some regions of the epitopes of the classes 2 and 3 of antibodies (Fig. 4a, b and
215 Supplementary Fig. 4a), the major 35B5-interacting residues, including the
216 SARS-CoV-2 specific residues N354, T470 and N481 (Fig. 3b), which are not
217 conserved in the spike proteins of SARS-CoV and MERS-CoV, are outside of the
218 epitopes of the classes 2 and 3 of antibodies. Therefore, 35B5 targets a distinctive
219 epitope to specifically neutralize SARS-CoV-2.

220 The SARS-CoV-2 VOCs contains several prevailing mutations on RBD,
221 including N501Y (B.1.1.7 (alpha), B.1.351 (beta), P1 (gamma) and B.1.1.529
222 (omicron)), K417N (B.1.351 (beta), P1 (gamma) and B.1.1.529 (omicron)), L452Q
223 (C.37 (lambda)), L452R (B.1.617.2 (delta), B.1.427/B.1.429 (epsilon), B.1.617.1

224 (kappa) and B.1.526 (iota)), S477N (B.1.526 (iota) and B.1.1.529 (omicron)), T478K
225 (B.1.617.2 (delta) and B.1.1.529 (omicron)), E484A (B.1.1.529 (omicron)), E484K
226 (B.1.351 (beta), P1 (gamma), B.1.617.2 (delta), B.1.525 (eta), and B.1.526 (iota)) and
227 F490S (C.37 (lambda)). Besides, newly reported B.1.1.529 (omicron) variant harbors
228 additional mutations on RBD (Fig. 5a). However, in the 35B5 Fab-S-6P complex
229 structures, the aforementioned residues (e.g., N501, K417, L452, S477, T478 and
230 F490) are not involved in the 35B5-RBD interactions. Only the residue E484 is
231 located at the edge of the 35B5-RBD interface but not contacted by 35B5 Fab (Fig. 4c
232 and Fig. 5b). Substitution of E484 by a lysine residue doesn't generate severe
233 structural collision with 35B5 Fab (Fig. 5c). It has been found that L452R mutation is
234 of significant adaptive value to the B.1.617.2 variant (delta). However, L452 has the
235 distance of more than 4.5 Å and 5.1 Å, respectively, to the residues T69 and Y60 of
236 35B5 Fab in the 35B5 Fab-S-6P complex structure (Fig. 5e), suggesting that the
237 residue is not contacted by 35B5 Fab. Substitution for L452 by an arginine does not
238 spatially affect the 35B5 Fab-RBD contacts. Instead, the mutation generates direct
239 interactions with the residues Y60 and T69 of 35B5 Fab within 3 Å and likely forms
240 two hydrogen bonds (Fig. 5e), suggesting that this mutation does not affect the
241 binding affinity of 35B5 to RBD. Consistently, 35B5 has the comparable super-potent
242 neutralization efficacy to the B.1.617.2 variant as that to the wild-type virus (Fig. 2).
243 Recently, it was found that the C.37 variant (lambda) contains the mutations L452Q
244 and F490S²⁸. However, the mutations L452Q and F490S would not structurally affect

245 the interactions of 35B5 Fab with RBD in the 35B5 Fab-S-6P complex structures (Fig.
246 5f, g), indicating that 35B5 might also exhibit potent neutralizing efficacy to the C.37
247 variant. Remarkably, we also found no direct contacts between 35B5 Fab and
248 mutations of the B.1.1.529 variant (omicron) (Supplementary Fig. 5), suggesting
249 35B5 might be able to neutralize the B.1.1.529 variant (omicron). Thus, the unique
250 epitope of 35B5 on RBD subtly avoids the prevailing mutation sites, which provides
251 the molecular basis for the potent pan-neutralizing efficacy of 35B5 to the
252 SARS-CoV-2 VOCs.

253

254 **Neutralization mechanism of mAb 35B5**

255 To investigate the neutralization mechanism of 35B5, we analyzed the “down” RBD
256 domain in the State 1 35B5 Fab-S-6P complex. In the density map of the State 1
257 complex, there were some residual densities closed to the “down” RBD domain. We
258 further carried out local refinements on the “down” RBD. The local refinements
259 generated a 4.8-Å density map and revealed that there is a 35B5 Fab contacting the
260 edge of the epitope on the “down” RBD. The low resolution of the local refinement
261 map suggests that the interaction between the 35B5 Fab and the “down” RBD is
262 highly dynamic (Supplementary Fig. 4b-e). Structural modeling after the local
263 refinements revealed that, in contrast to the neutralizing mAbs BD-368^{22, 23} and
264 C002²⁴ recognizing the epitopes that are fully exposed in both “down” and “up”
265 RBDs, 35B5 Fab utilizes the CDRH regions to interact with the residues E340, T345,

266 R346, F347, R346, K444, Y449 and N450 at the exposed edge of the epitope on the
267 “down” RBD, indicating that this RBD domain is being initially recognized by 35B5
268 (Fig. 4d and Supplementary Fig. 4e and Supplementary Fig. 8a, c). Structural
269 superimposition of the 35B5 Fab-“up” RBD model with the “down” RBD in the 35B5
270 Fab-S-6P complex of State 1 or those in the Fab-free spike trimers^{22, 29} reveals that the
271 β -sheet and the linking loop of FRH1 of 35B5 Fab have severe structural clashes with
272 the adjacent NTD domain of the spike protein (Fig. 4e), suggesting that upon the
273 high-affinity binding of 35B5 Fab onto the “down” RBD, the spatial collisions
274 between 35B5 Fab and the NTD domain potentially exert repulsion force onto the
275 NTD domain to induce the conformational conversion of RBD from “down” to “up”
276 conformation. Further outward movement of the “up” RBDs generated the “releasing”
277 conformations in the State 3 35B5 Fab-S-6P complex. Thus, the 35B5 Fab-S-6P
278 complex structures in these three states suggest that neutralization of SARS-CoV-2 by
279 35B5 is likely carried out in four sequential steps (Fig. 4g): 35B5 firstly binds to the
280 exposed edge of the epitope to recognizes the “down” RBDs of the spike protein;
281 subsequently, binding of 35B5 imposes structural clashes on the NTD domain to drive
282 the conformational changes of RBDs from “down” to “up”; next, the unstable “up”
283 conformations of the RBD domains destabilizes the structure of the spike trimer and
284 induces the outward movement and releasing of RBDs; finally, the released RBD
285 domains cause the dissociation of the spike trimer.

286 The SARS-CoV-2 VOCs contains the most prevalent mutation D614G in the

287 spike protein, which enhances infectivity by inducing the wedge of a disordered loop
288 between the SD1/CTD1 and NTD domains within a protomer to prevent premature
289 dissociation of the G614 trimer³⁰. The residue D614 is not located in the epitope of
290 35B5 (Fig. 3b), thereby having no effects on its binding to the RBD domain.
291 Moreover, upon binding to the “down” RBD domain, the capability of 35B5 to exert
292 the repulsion force onto the NTD domain can counteract the effects of the D614G
293 mutation on the structural arrangement of the spike protein. Therefore, the unique
294 epitope of 35B5 avoiding the prevailing mutation sites on RBD and the repulsion
295 force of 35B5 exerting onto NTD during initial recognition renders its super-potent
296 pan-neutralizing efficacy to the SARS-CoV-2 VOCs.

297

298 **Cryo-EM structure of mAb 32C7**

299 In contrast to 35B5, mAb 32C7 could not efficiently neutralize the SARS-CoV-2
300 VOCs. We also solved the cryo-EM structure of the Fab region of mAb 32C7
301 (hereafter named as 32C7 Fab) in complex with S-6P at a resolution of 2.8 Å
302 (Supplementary Fig. 6 and Supplementary Table 1). The complex structure only
303 contains one 32C7 Fab molecule, which is bound to a “down” RBD domain in the
304 spike protein (Supplementary Fig. 7a-f). The binding surface of 32C7 Fab on RBD
305 overlaps with the epitopes of the class 3 antibodies (Supplementary Fig. 7c),
306 suggesting that 32C7 belongs to the classic class 3 family of neutralizing antibodies.
307 The 32C7 Fab-RBD interface only covers a buried area of approximately 935 Å²,

308 which is much less than that of 35B5 Fab (Fig. 3c and Supplementary Fig. 7g and
309 Supplementary Fig. 8b, d). The smaller epitope surface on RBD determined the
310 weaker neutralization efficacy of 32C7 as compared to that of 35B5 (Fig. 1). In the
311 S-6P-32C7 Fab complex structure, 32C7 Fab does not structurally clash with the NTD
312 domain. Instead, 32C7 Fab interacts with the glycan moiety on the residue N165 of
313 the NTD domain (Supplementary Fig. 7b). In addition to the D614G mutation, the
314 B.1.351 variant harbors 4 amino acid substitutions and 1 deletion of 3 amino acids,
315 which cause the conformational change of the NTD domain. The conformational
316 changes of the NTD domain potentially weaken the interactions of 32C7 Fab with the
317 glycan moiety of N165, and further affect its epitope recognition of RBD, thereby
318 impairing the neutralizing efficacy of 32C7 Fab against the B.1.351 and other VOCs.

319

320 **Discussion**

321 In this study, we demonstrate 35B5 as a ultrapotent and pan-neutralizing human
322 monoclonal antibody against currently circulating SARS-CoV-2 provided by
323 experimental evidence *in vitro* and *in vivo* as well as structural analysis. By contrast,
324 many mAbs such as casirivimab (REGN10933), bamlanivimab (LY-CoV555),
325 etesevimab (LY-CoV016), regdanvimab (CT-P59), ABBV-2B04 (2B04) and 32C7 in
326 the study partially or entirely lose the neutralizing activity against B.1.351 and
327 B.1.617.2^{2, 11, 31, 32}. The mechanisms underlying the picomolar broad neutralization by
328 35B5 at least involve three aspects: 1) broad interface and extensive interactions

329 between 35B5 and RBD endow 35B5 as a potent cross-epitope mAb; 2) proactive
330 dissociation of the spike trimer by structural clashes between 35B5 Fab FRH1 and
331 spike NTD domain; 3) no direct contacts between 35B5 Fab and prevailing mutations
332 of SARS-CoV-2 VOCs.

333 Previous works indicated that the ACE-binding surface is partially exposed on the
334 “down” RBDs in the tight- or loose-closed spike trimer^{22, 29}. The epitopes of some
335 neutralizing mAbs are also partially exposed on the “down” RBDs^{24, 33, 34, 35, 36}. The
336 35B5 Fab-S-6P complex structures in the three states we determined provide for the
337 first time the direct structural evidence for the possibility that the ACE2 or mAbs can
338 approach the partially exposed surface or epitope residues for initial recognition and
339 fulfil the conformational transformation of RBD. In previously identified
340 RBD-targeted mAbs, almost all class 1 mAbs interact extensively with the residues
341 K417 and N501. Most class 2 and class 3 mAbs contact E484, and most class 3 mAbs
342 interact with L452³. 35B5 does not directly bind to these prevailing mutant sites. In
343 contrast to the Class 3 mAb S309²⁷ and the Class 4 mAb CR3022³⁷, which target the
344 residues conserved in the spike proteins of SARS-CoV, SARS-CoV-2 and
345 MERS-CoV and therefore have cross-species neutralizing activities, 35B5 is a
346 SARS-CoV-2 specific antibody with super potent pan-neutralizing activities to
347 SARS-CoV-2 VOCs.

348 Protective vaccines are considered as keys to terminate the COVID-19 pandemic.
349 However, accumulating evidence suggests that SARS-CoV-2 VOCs compromise

350 neutralization by antibody responses induced by multiple vaccines^{13, 14, 15, 16, 38, 39, 40},
351 including mRNA vaccines (BNT162b2 and mRNA-1273), adenovirus-based vaccines
352 (AZD1222 and JNJ-78436735), a nanoparticle-based vaccine (NVX-CoV2373) and
353 an inactivated protein vaccine (Coronavac), primarily due to RBD mutations. Thus,
354 vaccines aimed at eliciting broadly neutralizing mAbs against SARS-CoV-2 VOCs are
355 urgently needed. In the scenario of coping with diverse HIV-1 variants, an
356 experimental pan-HIV-1 vaccine was designed based on the structurally defined
357 epitope of a HIV-1 neutralizing mAb N123-VRC34.01, which targets a linear peptide
358 of fusion peptide that is across-clade conserved^{41, 42}. In our study, cryo-EM structure
359 of neutralizing 35B5 to the SARS-CoV-2 spike revealed an epitope that is composed
360 of 30 residues and conserved among all the currently known SARS-CoV-2 VOCs
361 (especially B.1.617.2 (delta) and B.1.1.529 (omicron)). Importantly, mAb 35B5 was
362 cloned from SARS-CoV-2 RBD-specific B cells obtained from individuals during
363 their early convalescence, which might endow mAb 35B5 with limited somatic
364 hypermutation (SHM). In contrast, a broad neutralizing mAb, ADG-2, was engineered
365 by *in vitro* affinity optimization⁴³ and the extensive SHM makes ADG-2 epitope
366 challenging as a target for SARS-CoV-2 vaccines. Thus, we propose that the 35B5
367 epitope might be a valuable target for the rational design of a universal SARS-CoV-2
368 vaccine, which is presumably essential for the ultimate termination of COVID-19
369 pandemic in the future.

370

371 **Methods**

372 **Human samples.** The COVID-19 patients enrolled in the study were admitted to
373 Guangzhou Eighth People's Hospital (January to March 2020) and provided written
374 informed consent. Blood samples were collected from patients during their
375 convalescence and the time between symptom onset to sample collection was around
376 20 days. Healthy donors were 2 adult participants in the study. Blood samples were
377 collected in cell preparation tubes with sodium citrate (BD Bioscience). Then,
378 peripheral blood mononuclear cells (PBMCs) were isolated from blood samples using
379 Ficoll (TBD Science), washed with PBS, suspended in cell freezing medium (90%
380 FBS plus 10% DMSO), frozen in freezing chamber at -80 °C, and then transferred to
381 liquid nitrogen. The study received IRB approvals at Guangzhou Eighth People's
382 Hospital (KE202001134).

383

384 **Single-cell sorting, RT-PCR and PCR cloning.** PBMCs were firstly incubated with
385 Human TruStain FcX (Biolegend) at 4 °C for 30 min and then stained with
386 biotin-conjugated SARS-CoV-2 RBD protein (Sino Biological, 40592-V05H) at 4 °C
387 for 20 min. Next, PBMCs were stained with PE-Cy7-conjugated streptavidin
388 (eBioscience), FITC-conjugated anti-CD19 antibody (Biolegend), PE-conjugated
389 anti-CD20 antibody (Biolegend), APC-conjugated anti-human IgG (Fc) (Biolegend),
390 APC-Cy7-conjugated anti-CD3 antibody (Biolegend), APC-Cy7-conjugated
391 anti-CD14 antibody (Biolegend), APC-Cy7-conjugated anti-CD56 antibody
392 (Biolegend) and APC-Cy7-conjugated LIVE/DEAD dye (Life Technologies) at 4 °C
393 for 30 min. All the stainings were performed in PBS containing 5% mouse serum
394 (wt/vol). For cell sorting, the SARS-CoV-2 RBD-specific IgG⁺ B cells were sorted
395 into 96-well plates, with a single cell and 10 µl catch buffer per well. These plates
396 were stored at -80 °C for further usage. Catch buffer: to 1 ml of RNAase-free water
397 (Tiangen Biotech), add 40 µl Rnasin (NEB) and 50 µl 1.5 M Tris pH 8.8 (Beijing
398 Dingguo Changsheng Biotech).

399 IgG VH and VL genes from B cells were PCR amplified and cloned into vectors
400 as previously described^{44,45}. Briefly, plates containing cell lysate were thawed on ice,
401 added with RT-PCR master mix and IgG VH/VL primers per well and performed with
402 RT-PCR following the one step RT-PCR kit protocol (Takara, RR057A). Then,
403 RT-PCR products were nested PCR-amplified with primers for IgG VH or IgG VL
404 following the HS DNA polymerase kit protocol (Takara, TAK R010). The IgG VH
405 and IgG VL nested PCR products were purified and next cloned into human IgG1
406 heavy chain and light chain expression vectors, respectively.

407

408 **Monoclonal antibody production and purification.** Monoclonal antibodies were
409 produced by using the ExpiCHOTM Expression System (Thermo Fisher). Briefly,
410 ExpiCHO-STM cells of 200 ml (6×10^6 cells/ml) in 1-L flask were transfected with
411 master mixture containing 200 μ g heavy chain plasmid, 200 μ g light chain plasmid
412 and 640 μ l ExpiFectamineTM CHO reagent. On the day after transfection, cultured
413 cells were added with 1.2 ml ExpiCHOTM enhancer and 48 ml ExpiCHOTM feed. A
414 second volume of ExpiCHOTM feed was added into cultured cells on day 5
415 post-transfection. Supernatants were harvested on day 12 post-transfection for
416 antibody purification using rProtein A Sepharose affinity chromatography (Sigma).

417 **Cells and viruses.** Vero E6 cells were obtained from ATCC and maintained in
418 Dulbecco's Modified Essential Medium (DMEM) supplemented with 10% fetal
419 bovine serum (FBS) (ThermoFisher) and 1% penicillin-streptomycin (ThermoFisher)
420 at 37 °C with 5% CO₂. The WT SARS-CoV-2 virus (GDPCC-nCOV01, GISAID:
421 EPI_ISL_403934), the B.1.351 variant (SARS-CoV-2/human/CHN/20SF18530/2020
422 strain; GDPCC-nCOV84, National Genomics Data Center:
423 ACC_GD530_GZ_2020-12-10) and the B.1.617.2 variant (GDPCC 2.00096,
424 sequence has not been published) were obtained from the Guangdong Center for
425 Human Pathogen Culture Collection (GDPCC) at Guangdong Provincial Center for
426 Disease Control and Prevention. The D614G variant

427 (hCoV-19/CHN/SYSU-IHV/2020 strain; GISAID: EPI_ISL_444969) was isolated
428 from the sputum of a female infected individual and propagated in Vero E6 cells.

429

430 **Surface Plasmon Resonance (SPR) assay.** SPR experiments were performed using a
431 Biacore® T100 instrument (GE Healthcare, Uppsala, Sweden). All binding analyses
432 were performed at 25 °C using HBS-EP+ (10 mM HEPES, 150 mM NaCl, 3 mM
433 EDTA, 0.005% Tween-20) as the running buffer. Experiments were executed
434 following the previously described SPR protocol⁴⁶. Briefly, RBD protein was
435 immobilized on the sensor chip CM5-type surface raising a final immobilization level
436 of ~600 Resonance Units (RU). Serial dilutions of 35B5 were injected in
437 concentration from 10 to 0.625 nM. Serial dilutions of 32C7 were injected in
438 concentration from 120 to 7.5 nM. For the competitive binding assays, the first
439 sample flew over the chip at a rate of 20 µl/min for 120 s, then the second sample was
440 injected at the same rate for another 200 s. The response units were recorded at room
441 temperature and analyzed using the same software as mentioned above.

442

443 **ELISA.** The ELISA plates were coated with 50 ng of SARS-CoV-2 RBD protein
444 (Sino Biological, 40592-V08H) in 100 µl PBS per well overnight at 4 °C. On the next
445 day, the plates were incubated with blocking buffer (5% FBS + 0.1% Tween 20 in
446 PBS) for 1 hour. Then, serially diluted mAbs in 100 µl blocking buffer were added to
447 each well and incubated for 1 hour. After washing with PBST (PBS + 0.1% Tween 20),
448 the bound antibodies were incubated with HRP-conjugated goat anti-human IgG
449 antibody (Bioss Biotech) for 30 min, followed by washing with PBST and addition of
450 TMB (Beyotime). The ELISA plates were allowed to react for ~5 min and then
451 stopped by 1 M H₂SO₄ stop buffer. The optical density (OD) value was determined at
452 450 nm. EC₅₀ values were determined by using Prism 6.0 (GraphPad) software after
453 log transformation of the mAb concentration using sigmoidal dose-response nonlinear
454 regression analysis.

455

456 **Neutralization assay.** Infectious SARS-CoV-2 neutralization assay was performed
457 according to previous reports⁴⁷. Vero E6 cells were seeded in a 24-well culture plates
458 at a concentration of 4×10^4 cells per well at 37 °C for 24 h. For infection with
459 authentic SARS-CoV-2 at an MOI of 0.005, 200 μ l of diluted authentic SARS-CoV-2
460 and 5-fold serially diluted 35B5 or 32C7 (from 5 μ g/mL to 0.064 μ g/mL) mAbs were
461 mixed in the medium with 2% FBS, and were then added into the Vero E6 cells. The
462 culture supernatant was collected at 48h post-infection for focus forming assay and
463 qRT-PCR. IC₅₀ values were determined by nonlinear regression using Prism 6.0
464 (GraphPad).

465

466 **Focus forming assay (FFA).** The virus titer was detected by FFA, which is
467 characterized by its high-throughput as compared to the traditional plaque assay⁴⁸.
468 Briefly, Vero E6 cells were seeded in 96-well plates 24h prior to infection. Virus
469 cultures were serially diluted and used to inoculate Vero E6 cells at 37°C for 1 h,
470 followed by changed with fresh medium containing 1.6% carboxymethylcellulose.
471 After 24 hours, Vero E6 cells were fixed with 4% paraformaldehyde and
472 permeabilized with 0.5% Triton X-100. Cells were then incubated with
473 anti-SARS-CoV-2 nucleocapsid protein polyclonal antibody (Sino Biological),
474 followed by an HRP-labeled secondary antibody (Proteintech). The foci were
475 visualized by TrueBlue Peroxidase Substrate (SeraCare Life Science), and counted
476 with an ELISPOT reader.

477

478 **Protection against SARS-CoV-2 in hACE2 mice.** All animal experiments were
479 carried out in strict accordance with the guidelines and regulations of Laboratory
480 Monitoring Committee of Guangdong Province of China and were approved by
481 Ethics Committee of Zhongshan School of Medicine of Sun Yat-sen University on
482 Laboratory Animal Care (SYSU-IACUC-2021-00432). Viral infections were

483 performed in a biosafety level 3 (BSL3) facility in accordance with recommendations
484 for the care and use of laboratory animals. The hACE2 mice of the same sex were
485 randomly assigned to each group. For infection, ICR-hACE2 mice were anesthetized
486 with isoflurane and inoculated intranasally with 4×10^4 PFU SARS-CoV-2 virus
487 (GISAID: EPI_ISL_402125). Six hours later, the infected mice received a single dose
488 of 35B5 (20 mg/kg) or 32C7 (20 mg/kg) or vehicle. And the H11-K18-hACE2 mice
489 were intranasally challenged with 4×10^4 PFU of three subtypes SARS-CoV-2 virus
490 (D614G, B.1.351 and B.1.617.2) per mouse, respectively. Four hours later, the
491 infected mice received a single dose of 35B5 (30 mg/kg) or vehicle. The lungs were
492 collected at day 5 post-infection for further assays.

493

494 **Measurement of viral burden.** For *in vitro* neutralization assay, RNA of culture
495 supernatant was extracted by using TRIzol reagent (Invitrogen). For *in vivo*
496 neutralization assay, lungs of SARS-CoV-2 infected mice were collected and
497 homogenized with gentle MACS M tubes (Miltenyi Biotec, 130-093-236) in a gentle
498 MACS dissociator (Miltenyi Biotec, 130-093-235). Then, total RNA of homogenized
499 lung tissues was extracted with RNeasy Mini Kit (QIAGEN, 74104) according to the
500 manufacturer's instruction. The extracted RNA was performed with quantitative
501 RT-PCR (qRT-PCR) assay to determine the viral RNA copies by using one-step
502 SARS-CoV-2 RNA detection kit (PCR-Fluorescence Probing) (Da An Gene Co.,
503 DA0931).

504 To generate a standard curve, the SARS-CoV-2 nucleocapsid (N) gene was
505 cloned into a pcDNA3.1 expression plasmid and *in vitro* transcribed to obtain RNAs
506 for standards. Indicated copies of N standards were 10-fold serially diluted and
507 proceeded to qRT-PCR utilizing the same one-step SARS-CoV-2 RNA detection kit to
508 obtain standard curves. The reactions were carried out on a QuantStudio 7 Flex
509 System (Applied Biosystems) according to the manufacturer's instruction under the
510 following reaction conditions: 50 °C for 15 min, 95 °C for 15 min, and 45 cycles of

511 94 °C for 15 s and 55 °C for 45 s. The viral RNA copies of each tissue were calculated
512 into copies per ml and presented as log₁₀ scale. The N specific primers and probes
513 were: N-F (5'- CAGTAGGGGAACTTCTCCTGCT-3'), N-R
514 (5'-CTTTGCTGCTGCTTGACAGA-3') and N-P
515 (5'-FAM-CTGGCAATGGCGGTGATGCTGC-BHQ1-3'). In each qRT-PCR
516 experiment, both positive control and negative control of simulated RNA virus
517 particles were included to monitor the entire experimental process and ensure the
518 reliability of the test results.

519

520 **Quantification of cytokine and chemokine mRNA.** RNA was isolated from lung
521 homogenates as described above. Then, cDNA was synthesized from isolated RNA
522 using HiScript III RT SuperMix for qPCR (Vazyme Biotech). The mRNA expression
523 levels of cytokine and chemokine were determined by using ChamQ Universal SYBR
524 q-PCR Master Mix (Vazyme Biotech) with primers for *IL-6* (forward:
525 CCCCAATTTCCAATGCTCTCC; reverse: CGCACTAGGTTTGCCGAGTA), *IL-1b*
526 (forward: TCGCTCAGGGTCACAAGAA; reverse: GTGCTGCCTAATGTCCCCTT),
527 *Tnfa* (forward: ATGGCTCAGGGTCCAACCTCT; reverse:
528 CGAGGCTCCAGTGAATTCGG), *Ccl2* (forward: AACTGCATCTGCCCTAAGGT;
529 reverse: AGGCATCACAGTCCGAGTCA) and *Cxcl1* (forward:
530 ACTCAAGAATGGTCGCGAGG; reverse: GTGCCATCAGAGCAGTCTGT). The
531 results were normalized to *Gapdh* levels.

532

533 **Histopathology.** At day 5 post-SARS-CoV-2 infection, hACE2 mice were euthanized,
534 and lungs were collected and fixed in 4% paraformaldehyde buffer. Tissues were
535 embedded with paraffin and sections (3-4 mm) were stained with hematoxylin and
536 eosin (H&E).

537

538 **Production and purification of S-2P and S-6P proteins.** The plasmids encoding the
539 ectodomains of the SARS-CoV-2 S-2P and S-6P mutants were kindly provided by Dr.
540 Junyu Xiao. HEK293F cells were cultured in the SMM 293-TI medium (Sino
541 Biological Inc.) at 37 °C with 8% CO₂. The S-2P and S-6P plasmids were transiently
542 transfected into HEK293F cells using 25-kDa linear polyethyleneimine (PEI)
543 (Polysciences) with the PEI:DNA mass ratio of 3:1 and 1 mg DNA for per liter of
544 culture when the cell density reached 2×10^6 cells per mL. At day 4 post-transfection,
545 the supernatants of the cell culture were harvested by centrifugation at $10,000 \times g$ for
546 30 min. The secreted S-2P and S-6P proteins were purified using HisPurTM cobalt
547 resins (Thermo Scientific) and StrepTactin resins (IBA). Further purification was
548 carried out using size-exclusion chromatography with a Superose 6 10/300 column
549 (GE Healthcare) in the buffer containing 20 mM HEPES pH 7.2, 150 mM NaCl and
550 10% Trehalose. The Fab regions of the 35B5 and 32C7 were obtained after the
551 digestion by papain for 40 min at 37 °C in a buffer containing 20 mM HEPES pH 7.2,
552 150 mM NaCl, 5 mM EDTA and 5 mM L-cysteine. The obtained Fabs were purified
553 with a Desalting column (GE Healthcare Life Sciences) to remove L-cysteine, and
554 then further purified in a HiTrap Q column (GE Healthcare Life Sciences). The
555 purified Fabs were collected and concentrated to 0.6 mg/mL.

556

557 **Negative staining analysis.** For negative-staining assays, the S-2P, S-6P, 35B5 Fab
558 and 32C7 Fab proteins were diluted to 0.02 mg/ml in the buffer of 20 mM HEPES,
559 pH 7.2, and 150 mM NaCl. 2 μ L of 35B5 Fab or 32C7 Fab was mixed with 2 μ L S-2P
560 or S-6P and incubated on ice for 3 and 10 min, respectively, or at room temperature
561 for 30 min. The samples were loaded in the glow-discharged carbon-coated copper
562 grids and stained with 3% Uranyl Acetate (UA). The prepared grids were examined
563 using a Tecnai G2 Spirit BioTWIN transmission electron microscope (FEI) operated
564 at 120 kV. Micrographs were recorded and analyzed using Digital Micrograph
565 software with 120,000 \times nominal magnification.

566

567 **Cryo-EM sample preparation and data collection.** 2 μL of S-6P (1.2 mg/mL) and 2
568 μL of 35B5 Fab or 32C7 Fab (0.6 mg/mL) were incubated for 3 min at room
569 temperature and then loaded onto the glow-discharged holy-carbon gold grids
570 (Quantifoil, R1.2/1.3). The grids were washed using the buffer containing 20 mM
571 HEPES, pH 7.2, and 150 mM NaCl. The washed grids were blotted using a Mark IV
572 Vitrobot (Thermo Fisher) at 100% humidity and 16 $^{\circ}\text{C}$ for 3 s, and *submerged in*
573 *liquid ethane by plunge-freezing*. For the S-6P-35B5 Fab complex, micrographs were
574 recorded on a FEI Titan Krios (Thermo Fisher) electron microscope operated at 300
575 kV. Totally, 3740 movies were recorded on a K3 Summit direct electron detector
576 (Gatan) in the super-resolution mode (0.5475 $\text{\AA}/\text{pixel}$) at a nominal magnification of
577 81,000 using a defocus range of 1.2 to 1.3 μm . A GIF Quantum energy filter (Gatan)
578 with a slit width of 20 eV was used on the detector. The micrographs were
579 dose-fractionated into 32 frames with a total electron exposure of ~ 50 electrons per \AA^2 .

580 For the S-6P-32C7 Fab complex, micrographs were collected on a FEI Titan Krios
581 (Thermo Fisher) operating at 300 kV using the AutoEMation software⁴⁹. Totally,
582 2528 movies were recorded on a K3 Summit direct electron detector (Gatan) in the
583 super-resolution mode (0.53865 $\text{\AA}/\text{pixel}$) at a nominal magnification of 81,000 using a
584 defocus range of 1.4 to 1.8 μm . A GIF Quantum energy filter (Gatan) with a slit width
585 of 20 eV was used on the detector. The micrographs were dose-fractionated into 32
586 frames with a total electron exposure of ~ 50 electrons per \AA^2 .

587

588 **Cryo-EM image processing.** Raw movie frames were binned, aligned and averaged
589 into motion-corrected summed images using MotionCor2⁵⁰. The dose-weighted
590 images were then imported into cryoSPARC⁵¹ for the following image processing,
591 including CTF estimation, particle picking and extraction, 2D classification, *ab initio*
592 3D reconstruction, heterogeneous 3D refinement and non-uniform homogeneous
593 refinement. For the S-6P-35B5 Fab complex, 8 representative particle templates were

594 generated in 2D classification of 65,242 particles auto-picked by the blob picker from
595 the first 1000 micrographs. Using these templates, 1,178,527 particles were extracted
596 with a box size of 330×330 and classified into 150 classes in 2D classification.
597 Among them, 43 classes that included 818,470 particles were selected for *ab initio* 3D
598 reconstruction and heterogeneous refinement. Finally, 392,378 particles reconstructed
599 an apparent architecture of the S-6p-35B5 Fab complex and were subjected to two
600 more rounds of *ab initio* 3D reconstruction and heterogeneous refinement before
601 non-uniform refinement. Then the particles were subjected to global and local CTF
602 refinement for final non-uniform refinement, and generated three abundant
603 populations of the S-6P-35B5 Fab complex and structures. Local refinements of the
604 RBD-35B5 Fab region were performed to improve the interface density in
605 *cryoSPARC*. Sharpened maps were generated and validated for model building and
606 refinement. Reported resolutions are based on the gold-standard Fourier shell
607 correlation^{52, 53} of 0.143 criterion.

608 For the S-6P-32C7 Fab complex, 4 representative particle templates were
609 generated in 2D classification of 122,851 particles auto-picked by the blob picker
610 from the first 1000 micrographs. Based on these templates, 744,865 particles were
611 extracted with a box size of 380×380 and classified into 150 2D classes. Among them,
612 28 classes including 338,454 particles were selected for *ab initio* 3D reconstruction
613 and heterogeneous refinement. 125,858 particles that reconstructed an apparent
614 architecture of the S-6P-32C7 Fab complex were subjected to two more rounds of *ab*
615 *initio* 3D reconstruction and heterogeneous refinement before non-uniform refinement.
616 Finally, the S-6P-32C7 Fab complex structure that only includes a bound 32C7 Fab
617 was reconstructed from 119,062 particles. Local refinement of the RBD-32C7 Fab
618 region was also performed.

619

620 **Cryo-EM structure modeling and analysis.** To build the S-6P-35B5 Fab complex
621 structural model, an “up” RBD-35B5 Fab model were first generated using a Fab

622 structure (PDB ID: 2X7L) and a RBD model from the Spike trimer (PDB ID: 7K8Y)
623 and manually built in Coot⁵⁴ in the locally refined map. The obtained RBD-35B5 Fab
624 model was superimposed with the intact Spike trimer structure (PDB ID: 7K8Y) to
625 generate an initial model of the S-6P-35B5 Fab complex model. The “down”
626 RBD-35B5 Fab model was obtained from fitting the structures of 35B5 Fab, the RBD
627 and NTD domains into the locally refined map of the the S-6P-35B5 Fab complex of
628 State 1 and then validated by *Phenix*⁵⁵. The model building of the S-6P-32C7 Fab
629 complex was carried out in the similar procedure as that of the S-6P-35B5 Fab
630 complex with a Spike trimer structure (PDB ID: 6XKL) as a template. All model
631 building were performed in Coot⁵⁴. Structural refinement and validation were carried
632 out in *Phenix*⁵⁵. Structural figures were generated using UCSF ChimeraX version
633 1.2⁵⁶.

634

635 **Statistics.** In the mouse study assessing mAb protection against WT SARS-CoV-2,
636 the comparisons of lung viral titers and lung cytokine/chemokine mRNA were
637 performed using one-way ANOVA with Tukey’s post hoc test by Prism 6.0
638 (GraphPad). In the mouse study assessing mAb protection against SARS-CoV-2
639 VOCs, the comparison of lung viral titers was performed using t test (unpaired) by
640 Prism 6.0 (GraphPad).

641

642 **Data and materials availability.** The cryo-EM maps and atomic coordinates have
643 been deposited to the Electron Microscopy Data Bank (EMDB) and Protein Data
644 Bank (PDB) with accession codes EMD-31033 and PDB 7E9N (State 1 of the 35B5
645 Fab-S-6P complex), EMD-31444 and PDB 7F46 (“down” RBD/35B5 Fab local

646 refinement of State 1), EMD-31034 and PDB 7E9O (State 2 of the 35B5 Fab-S-6P
647 complex), EMD-31035 and PDB 7E9P (“up” RBD/35B5 Fab local refinement of
648 State 2), EMD-31036 and PDB 7E9Q (State 3 of the 35B5 Fab-S-6P complex),
649 EMD-31209 and PDB 7ENF (the 32C7 Fab-S-6P complex), and EMD-31210 and
650 PDB 7ENG (“down” RBD/32C7 Fab local refinement).

651

652 **References**

- 653 1. World Health Organization. Weekly epidemiological update on COVID-19 -
654 23 November 2021.
655 <https://www.who.int/publications/m/item/weekly-epidemiological-update-on-covid-19---23-november-2021>.
656
657
- 658 2. Corti D, Purcell LA, Snell G, Veesler D. Tackling COVID-19 with
659 neutralizing monoclonal antibodies. *Cell*.
660
- 661 3. Yuan M, *et al.* Structural and functional ramifications of antigenic drift in
662 recent SARS-CoV-2 variants. *Science (New York, NY)*, (2021).
663
- 664 4. Volz E, *et al.* Evaluating the Effects of SARS-CoV-2 Spike Mutation D614G
665 on Transmissibility and Pathogenicity. *Cell* **184**, 64-75.e11 (2021).
666
- 667 5. Davies NG, *et al.* Estimated transmissibility and impact of SARS-CoV-2
668 lineage B.1.1.7 in England. *Science (New York, NY)* **372**, (2021).
669
- 670 6. Tegally H, *et al.* Detection of a SARS-CoV-2 variant of concern in South
671 Africa. *Nature* **592**, 438-443 (2021).
672
- 673 7. Faria NR, *et al.* Genomics and epidemiology of the P.1 SARS-CoV-2 lineage
674 in Manaus, Brazil. *Science (New York, NY)* **372**, 815-821 (2021).
675
- 676 8. Cherian S, *et al.* Convergent evolution of SARS-CoV-2 spike mutations,
677 L452R, E484Q and P681R, in the second wave of COVID-19 in Maharashtra,
678 India. *bioRxiv : the preprint server for biology*, (2021).
679
- 680 9. Callaway E. Heavily mutated Omicron variant puts scientists on alert. *Nature*,

- 681 (2021).
682
- 683 10. Chen RE, *et al.* Resistance of SARS-CoV-2 variants to neutralization by
684 monoclonal and serum-derived polyclonal antibodies. *Nature medicine*,
685 (2021).
686
- 687 11. Hoffmann M, *et al.* SARS-CoV-2 variants B.1.351 and P.1 escape from
688 neutralizing antibodies. *Cell*, (2021).
689
- 690 12. Hoffmann M, *et al.* SARS-CoV-2 variant B.1.617 is resistant to Bamlanivimab
691 and evades antibodies induced by infection and vaccination. *bioRxiv : the*
692 *preprint server for biology*, (2021).
693
- 694 13. Garcia-Beltran WF, *et al.* Multiple SARS-CoV-2 variants escape
695 neutralization by vaccine-induced humoral immunity. *Cell* **184**,
696 2372-2383.e2379 (2021).
697
- 698 14. Edara VV, *et al.* Infection- and vaccine-induced antibody binding and
699 neutralization of the B.1.351 SARS-CoV-2 variant. *Cell host & microbe* **29**,
700 516-521.e513 (2021).
701
- 702 15. Wu K, *et al.* Serum Neutralizing Activity Elicited by mRNA-1273 Vaccine.
703 *The New England journal of medicine* **384**, 1468-1470 (2021).
704
- 705 16. Wang Z, *et al.* mRNA vaccine-elicited antibodies to SARS-CoV-2 and
706 circulating variants. *Nature*, (2021).
707
- 708 17. Chen X, *et al.* Disease severity dictates SARS-CoV-2-specific neutralizing
709 antibody responses in COVID-19. *Signal transduction and targeted therapy* **5**,
710 180 (2020).
711
- 712 18. Sokal A, *et al.* Maturation and persistence of the anti-SARS-CoV-2 memory B
713 cell response. *Cell*, (2021).
714
- 715 19. Bao L, *et al.* The pathogenicity of SARS-CoV-2 in hACE2 transgenic mice.
716 *Nature* **583**, 830-833 (2020).
717
- 718 20. Sun SH, *et al.* A Mouse Model of SARS-CoV-2 Infection and Pathogenesis.
719 *Cell host & microbe* **28**, 124-133.e124 (2020).
720
- 721 21. Wrapp D, *et al.* Cryo-EM structure of the 2019-nCoV spike in the prefusion
722 conformation. *Science (New York, NY)* **367**, 1260-1263 (2020).

- 723
724 22. Hsieh CL, *et al.* Structure-based design of prefusion-stabilized SARS-CoV-2
725 spikes. *Science (New York, NY)* **369**, 1501-1505 (2020).
726
727 23. Du S, *et al.* Structurally Resolved SARS-CoV-2 Antibody Shows High
728 Efficacy in Severely Infected Hamsters and Provides a Potent Cocktail Pairing
729 Strategy. *Cell* **183**, 1013-1023 e1013 (2020).
730
731 24. Barnes CO, *et al.* SARS-CoV-2 neutralizing antibody structures inform
732 therapeutic strategies. *Nature* **588**, 682-687 (2020).
733
734 25. Benton DJ, *et al.* Receptor binding and priming of the spike protein of
735 SARS-CoV-2 for membrane fusion. *Nature* **588**, 327-330 (2020).
736
737 26. Lan J, *et al.* Structure of the SARS-CoV-2 spike receptor-binding domain
738 bound to the ACE2 receptor. *Nature* **581**, 215-220 (2020).
739
740 27. Pinto D, *et al.* Cross-neutralization of SARS-CoV-2 by a human monoclonal
741 SARS-CoV antibody. *Nature* **583**, 290-295 (2020).
742
743 28. Romero PE, *et al.* The Emergence of SARS-CoV-2 Variant Lambda (C.37) in
744 South America. *medRxiv : the preprint server for health sciences*, (2021).
745
746 29. Toelzer C, *et al.* Free fatty acid binding pocket in the locked structure of
747 SARS-CoV-2 spike protein. *Science (New York, NY)* **370**, 725-730 (2020).
748
749 30. Zhang J, *et al.* Structural impact on SARS-CoV-2 spike protein by D614G
750 substitution. *Science (New York, NY)* **372**, 525-530 (2021).
751
752 31. Dejnirattisai W, *et al.* Antibody evasion by the P.1 strain of SARS-CoV-2. *Cell*
753 **184**, 2939-2954.e2939 (2021).
754
755 32. Wang P, *et al.* Increased resistance of SARS-CoV-2 variant P.1 to antibody
756 neutralization. *Cell host & microbe* **29**, 747-751.e744 (2021).
757
758 33. Lv Z, *et al.* Structural basis for neutralization of SARS-CoV-2 and SARS-CoV
759 by a potent therapeutic antibody. *Science (New York, NY)* **369**, 1505-1509
760 (2020).
761
762 34. Tortorici MA, *et al.* Ultrapotent human antibodies protect against
763 SARS-CoV-2 challenge via multiple mechanisms. *Science (New York, NY)* **370**,
764 950-957 (2020).

- 765
766 35. Huo J, *et al.* Neutralization of SARS-CoV-2 by Destruction of the Prefusion
767 Spike. *Cell host & microbe* **28**, 497 (2020).
768
- 769 36. Asarnow D, *et al.* Structural insight into SARS-CoV-2 neutralizing antibodies
770 and modulation of syncytia. *Cell* **184**, 3192-3204 e3116 (2021).
771
- 772 37. Yuan M, *et al.* A highly conserved cryptic epitope in the receptor binding
773 domains of SARS-CoV-2 and SARS-CoV. *Science (New York, NY)* **368**,
774 630-633 (2020).
775
- 776 38. Cohen J. South Africa Suspends Use of AstraZeneca's COVID-19 Vaccine
777 after It Fails to Clearly Stop Virus Variant. *Science Magazine*, February 7,
778 2021.
779 [https://www.sciencemag.org/news/2021/02/south-africa-suspendsuse-astrazen](https://www.sciencemag.org/news/2021/02/south-africa-suspendsuse-astrazenecas-covid-19-vaccine-after-it-fails-clearly-stop)
780 [ecas-covid-19-vaccine-after-it-fails-clearly-stop](https://www.sciencemag.org/news/2021/02/south-africa-suspendsuse-astrazenecas-covid-19-vaccine-after-it-fails-clearly-stop)., (2021).
781
- 782 39. Wang GL, *et al.* Susceptibility of Circulating SARS-CoV-2 Variants to
783 Neutralization. *The New England journal of medicine*, (2021).
784
- 785 40. Herper M, Branswell, H. New Data Shed Light on Efficacy of J&J's
786 Single-Dose Covid Vaccine. *Stat*, February 24, 2021. [https://www.statnews/](https://www.statnews.com/2021/02/24/new-data-shed-light-on-efficacy-of-jjs-single-dose-vaccineag)
787 [com/2021/02/24/new-data-shed-light-on-efficacy-of-jjs-single-dose-vaccineag](https://www.statnews.com/2021/02/24/new-data-shed-light-on-efficacy-of-jjs-single-dose-vaccineag)
788 [ainst-covid-19/](https://www.statnews.com/2021/02/24/new-data-shed-light-on-efficacy-of-jjs-single-dose-vaccineag). (2021).
789
- 790 41. Xu K, *et al.* Epitope-based vaccine design yields fusion peptide-directed
791 antibodies that neutralize diverse strains of HIV-1. *Nature medicine* **24**,
792 857-867 (2018).
793
- 794 42. Kong R, *et al.* Fusion peptide of HIV-1 as a site of vulnerability to neutralizing
795 antibody. *Science (New York, NY)* **352**, 828-833 (2016).
796
- 797 43. Rappazzo CG, *et al.* Broad and potent activity against SARS-like viruses by
798 an engineered human monoclonal antibody. *Science (New York, NY)* **371**,
799 823-829 (2021).
800
- 801 44. Chen X, *et al.* Human monoclonal antibodies block the binding of
802 SARS-CoV-2 spike protein to angiotensin converting enzyme 2 receptor.
803 *Cellular & molecular immunology* **17**, 647-649 (2020).
804
- 805 45. Smith K, *et al.* Rapid generation of fully human monoclonal antibodies
806 specific to a vaccinating antigen. *Nature protocols* **4**, 372-384 (2009).

- 807
808 46. Real-Fernández F, *et al.* Surface plasmon resonance-based methodology for
809 anti-adalimumab antibody identification and kinetic characterization.
810 *Analytical and bioanalytical chemistry* **407**, 7477-7485 (2015).
811
812 47. Ju B, *et al.* Human neutralizing antibodies elicited by SARS-CoV-2 infection.
813 *Nature* **584**, 115-119 (2020).
814
815 48. Sun J, *et al.* Generation of a Broadly Useful Model for COVID-19
816 Pathogenesis, Vaccination, and Treatment. *Cell* **182**, 734-743.e735 (2020).
817
818 49. Lei J, Frank J. Automated acquisition of cryo-electron micrographs for single
819 particle reconstruction on an FEI Tecnai electron microscope. *J Struct Biol*
820 **150**, 69-80 (2005).
821
822 50. Zheng SQ, Palovcak E, Armache JP, Verba KA, Cheng Y, Agard DA.
823 MotionCor2: anisotropic correction of beam-induced motion for improved
824 cryo-electron microscopy. *Nat Methods* **14**, 331-332 (2017).
825
826 51. Punjani A, Rubinstein JL, Fleet DJ, Brubaker MA. cryoSPARC: algorithms for
827 rapid unsupervised cryo-EM structure determination. *Nat Methods* **14**,
828 290-296 (2017).
829
830 52. Henderson R, *et al.* Outcome of the first electron microscopy validation task
831 force meeting. *Structure* **20**, 205-214 (2012).
832
833 53. Scheres SH, Chen S. Prevention of overfitting in cryo-EM structure
834 determination. *Nat Methods* **9**, 853-854 (2012).
835
836 54. Emsley P, Lohkamp B, Scott WG, Cowtan K. Features and development of
837 Coot. *Acta Crystallogr D Biol Crystallogr* **66**, 486-501 (2010).
838
839 55. Liebschner D, *et al.* Macromolecular structure determination using X-rays,
840 neutrons and electrons: recent developments in Phenix. *Acta Crystallogr D*
841 *Struct Biol* **75**, 861-877 (2019).
842
843 56. Pettersen EF, *et al.* UCSF ChimeraX: Structure visualization for researchers,
844 educators, and developers. *Protein science : a publication of the Protein*
845 *Society* **30**, 70-82 (2021).
846
847 **Acknowledgements:** We thank Guangdong Center for Human Pathogen Culture

848 Collection (GDPCC) for providing SARS-CoV-2 isolates. We thank Dr. Junyu Xiao
849 (Peking University) for providing the plasmids encoding the ectodomains of the
850 SARS-CoV-2 S-2P and S-6P mutants. This work was supported by grants from the
851 National Natural Science Fund for Distinguished Young Scholars (No. 31825011 to
852 L.Y.), the National Science and Technology Major Project (No.
853 2017ZX10202102-006-002 to L.Y.), Guangdong Innovative and Entrepreneurial
854 Research Team Program (2016ZT06S638 to K.D.), High-level Biosafety Laboratory
855 Construction and Operation Program of the Science and Technology Projects of
856 Guangdong Province of China to K.D., the National Natural Science Fund (81925024
857 to Y. Z.), the National Key Research and Development Program of China
858 (2017YFA0503900 to Y. Z.), and the Fundamental Research Funds for the Central
859 Universities to Y. Z..

860

861 **Author contributions:** X.C., S.Y., Z.P., Y.Y., Y.L., J.Z., L.G., J.Z., L.X. and Q.H.
862 collected the PBMC, isolated SARS-CoV-2 RBD-specific B cells and cloned the
863 antibodies; A.H., Y.Z., F.Y., J.Z., F.L., Y.S., F.H., X.Y., Y.P., L.T., H.Z., H.Z., J.H. and
864 H.Z. performed *in vitro* and *in vivo* SARS-CoV-2 virus neutralization assays; X.W.
865 and A.L. performed negative stainings and cryo-EM analyses. L.Y. designed the study
866 and analyzed the data with Y.Z., K.D., X.C., X.W. and A.H.; X.C. wrote the first draft
867 of the manuscript, which was edited by Y.Z., L.Y., K.D., X.W. and A.H.; Y.Z., K.D.
868 and L.Y. supervised the study.

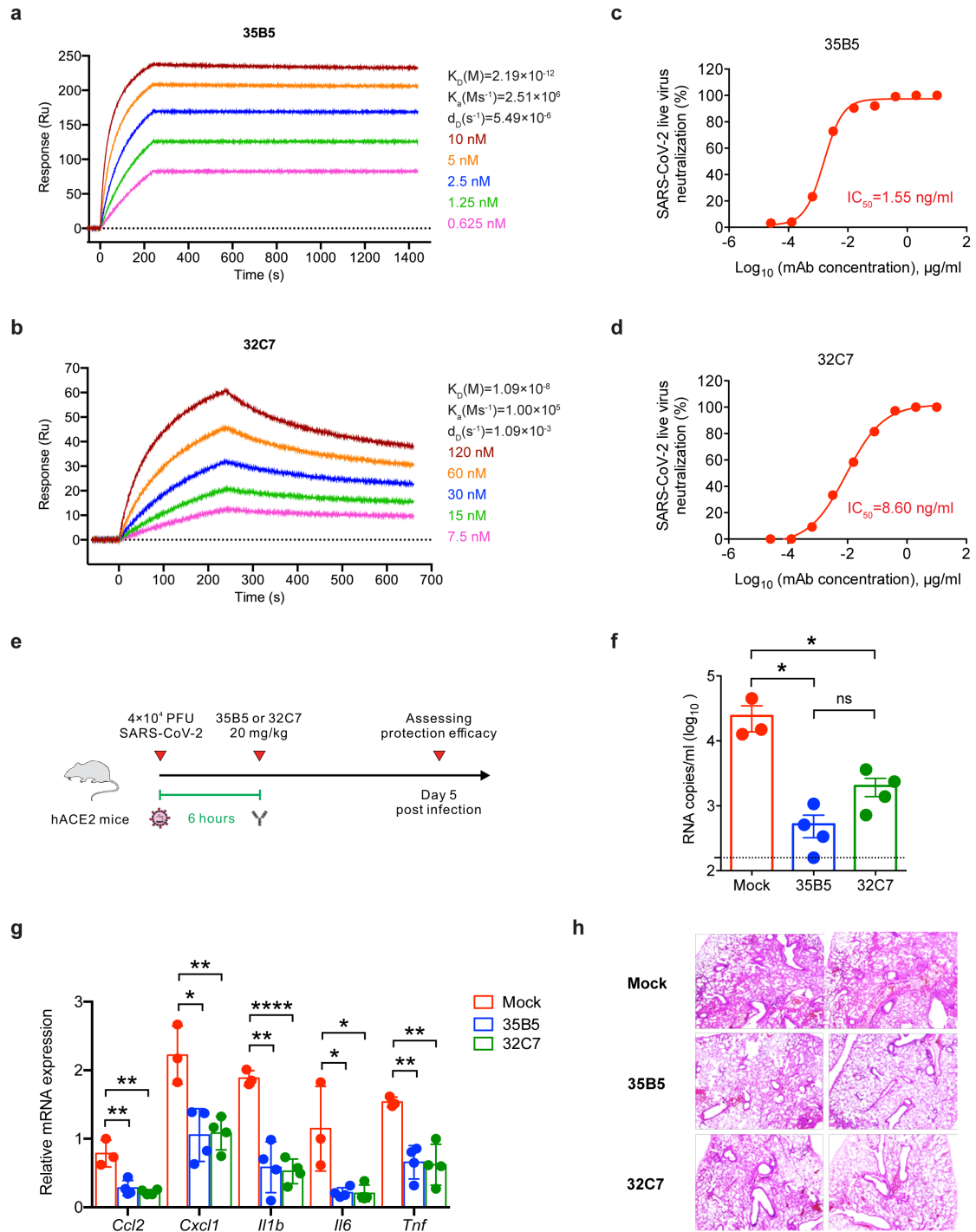
869

870 **Competing interests:** The pending patents of 35B5 and 32C7 have been licensed.

871 The authors declare no competing interests.

872

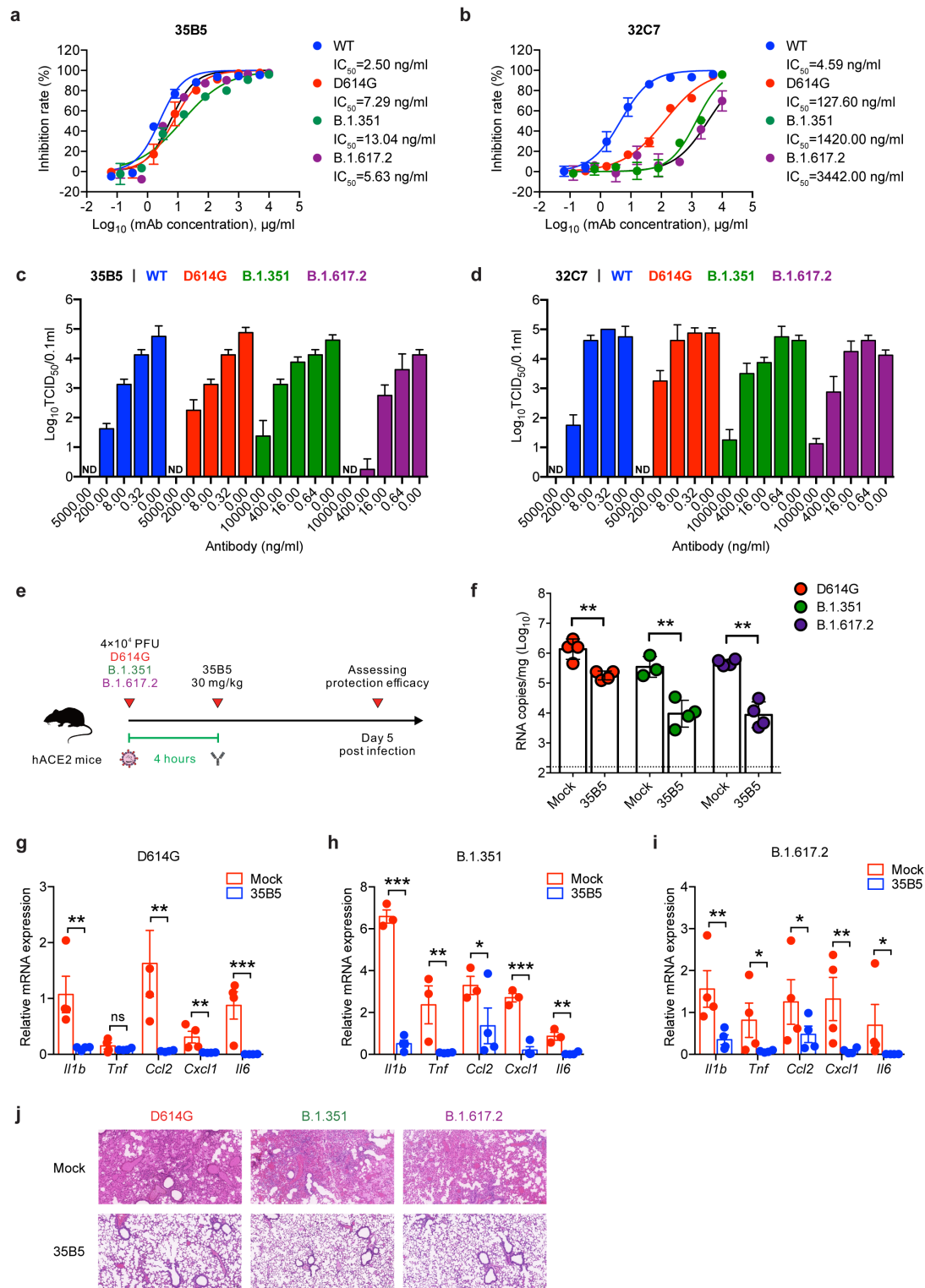
873 **Figure 1**



874
875

876 **Fig. 1 35B5 and 32C7 protect against authentic SARS-CoV-2 virus. a, b** Affinity
877 analysis of 35B5 (**a**) and 32C7 (**b**) binding to immobilized SARS-CoV-2 RBD by
878 using biolayer interferometry. **c, d** *In vitro* neutralizing activity of 35B5 (**c**) and 32C7
879 (**d**) against authentic SARS-CoV-2. Mixture of SARS-CoV-2 and serially diluted
880 35B5 or 32C7 were added to Vero E6 cells. After 48 hours, IC₅₀ values were
881 calculated by fitting the viral RNA copies from serially diluted mAb to a sigmoidal
882 dose-response curve. **e** Schematic diagram of 35B5 and 32C7 treatment *in vivo*. Six
883 hours after infection with 4×10^4 PFU SARS-CoV-2, the hACE2 mice received a
884 single dose of 35B5 or 32C7 with 20 mg/kg or no mAb treatment (mock). At day 5
885 post infection, lung tissues were collected for viral burden assessment,
886 cytokine/chemokine assay and histological analysis. **f** Viral titers in the lungs were
887 measured by qRT-PCR and presented as RNA copies per milliliter of lung abrasive
888 fluid. **g** Gene expressions of cytokines and chemokines in the lungs were determined
889 by qPT-PCR. **h** Histopathological analysis of lung tissues. The data are representative
890 of at least two independent experiments. * $P < 0.05$, ** $P < 0.01$ and **** $P < 0.0001$.
891 Not significant, ns. Error bars in (**f**) and (**g**) indicate SD.
892

893 **Figure 2**

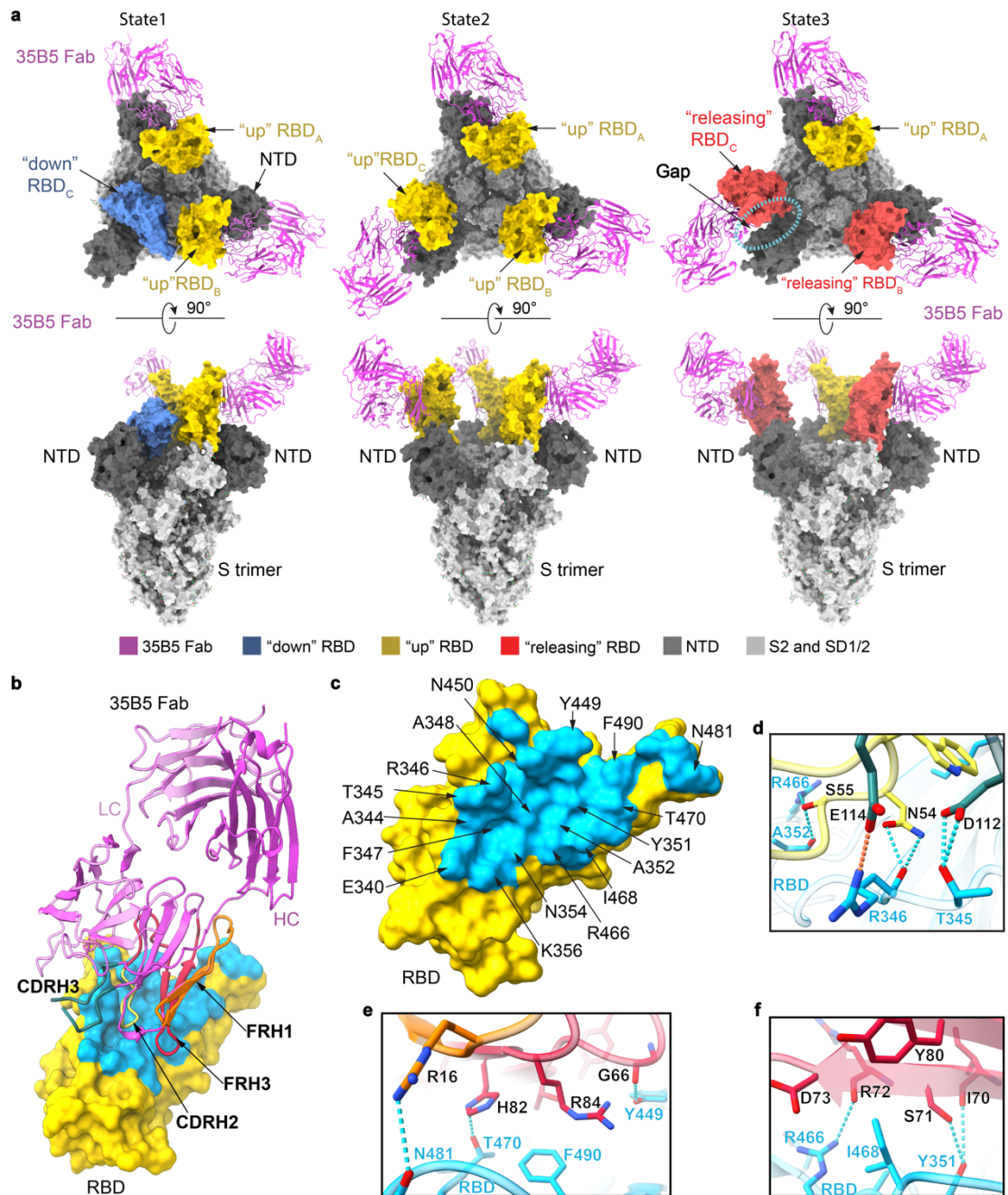


894

895

896 **Fig. 2 Neutralizing activity of 35B5 against SARS-CoV-2 VOCs. a, b** Neutralizing
897 activity of 35B5 (**a**) and 32C7 (**b**) against authentic SARS-CoV-2 viruses, including
898 WT strain, D614G variant, B.1.351 variant and B.1.617.2 variant. Mixture of each
899 SARS-CoV-2 strain and serially diluted 35B5 or 32C7 were added to Vero E6 cells.
900 After 48 hours, IC_{50} values were calculated by fitting the viral RNA copies from
901 serially diluted mAb to a sigmoidal dose-response curve. (**c, d**) FFA analysis of 35B5
902 (**c**) and 32C7 (**d**) against WT SARS-CoV-2, D614G variant, B.1.351 variant and
903 B.1.617.2 variant. Virus cultures were serially diluted and added to Vero E6 cells.
904 After 24 hours, the foci were visualized by using HRP-conjugated polyclonal
905 antibodies targeting SARS-CoV-2 nucleocapsid protein in Vero E6 cells and counted
906 with a ELISPOT reader. **e** Schematic diagram of 35B5 treatment *in vivo*. Four hours
907 after infection with 4×10^4 PFU SARS-CoV-2 D614G or B.1.351 or B.1.617.2, the
908 hACE2 mice received a single dose of 35B5 with 30 mg/kg or no mAb treatment
909 (mock). At day 5 post infection, lung tissues were collected for viral burden
910 assessment. **f** Viral titers in the lungs were measured by qRT-PCR and presented as
911 RNA copies per gram of lung tissue. **g to i** Gene expressions of cytokines and
912 chemokines in the lungs were determined by qPT-PCR. **j** Histopathological analysis
913 of lung tissues. ND, not detected. Data are representative of two independent
914 experiments. Error bars in **a-d, f-i** indicate SD.
915

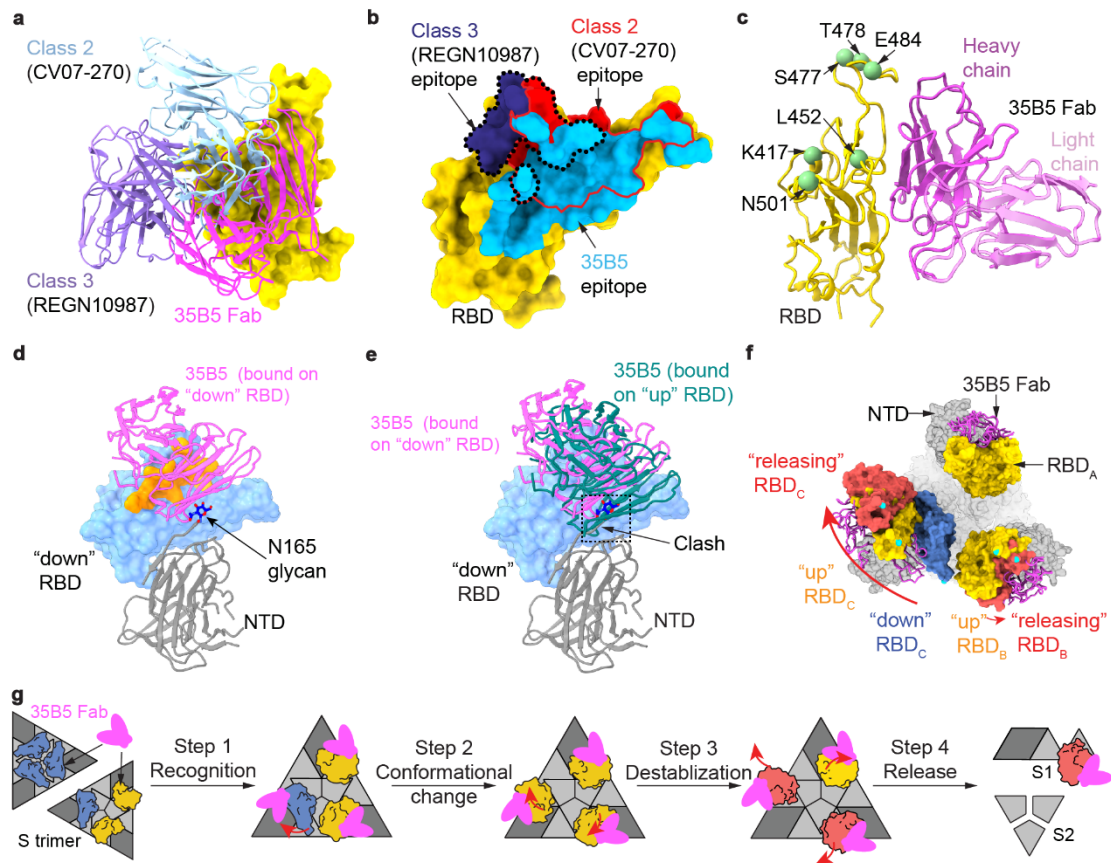
916 **Figure 3**



917
918

919 **Fig. 3 Cryo-EM structures of the spike protein S-6P complexed with 35B5 Fab. a**
920 The structures of the S-6P-35B5 Fab complex in three states. The S trimer is
921 represented as surface. 35B5 Fab is shown in cartoon and colored in purple. The
922 “down”, “up” and “releasing” RBD domains are colored in blue, yellow and red,
923 respectively. The NTD domain of the S trimer is colored in deep grey. The SD1, SD2
924 and S2 domains are colored in light grey. The gap caused by 35B5 Fab between the
925 “releasing” RBD and NTD domains is highlighted with dashed lines. **b** Interactions of
926 35B5 Fab with “up” RBD. The interacting residues within 4 Å in RBD are colored in
927 cyan. The RBD-interacting regions CDRH2, CDRH3, FRH1 and FRH3 of 35B5 Fab
928 are colored in yellow, blue, orange and red, respectively. **c**, The 35B5 epitope on RBD.
929 The epitope residues are labeled as indicated. **d-f** Detailed interactions of the CDR (**d**)
930 and FR regions (**e** and **f**) of 35B5 Fab with RBD. Hydrogen-bond and salt-bridge
931 interactions are shown as blue and orange dashed lines, respectively.
932

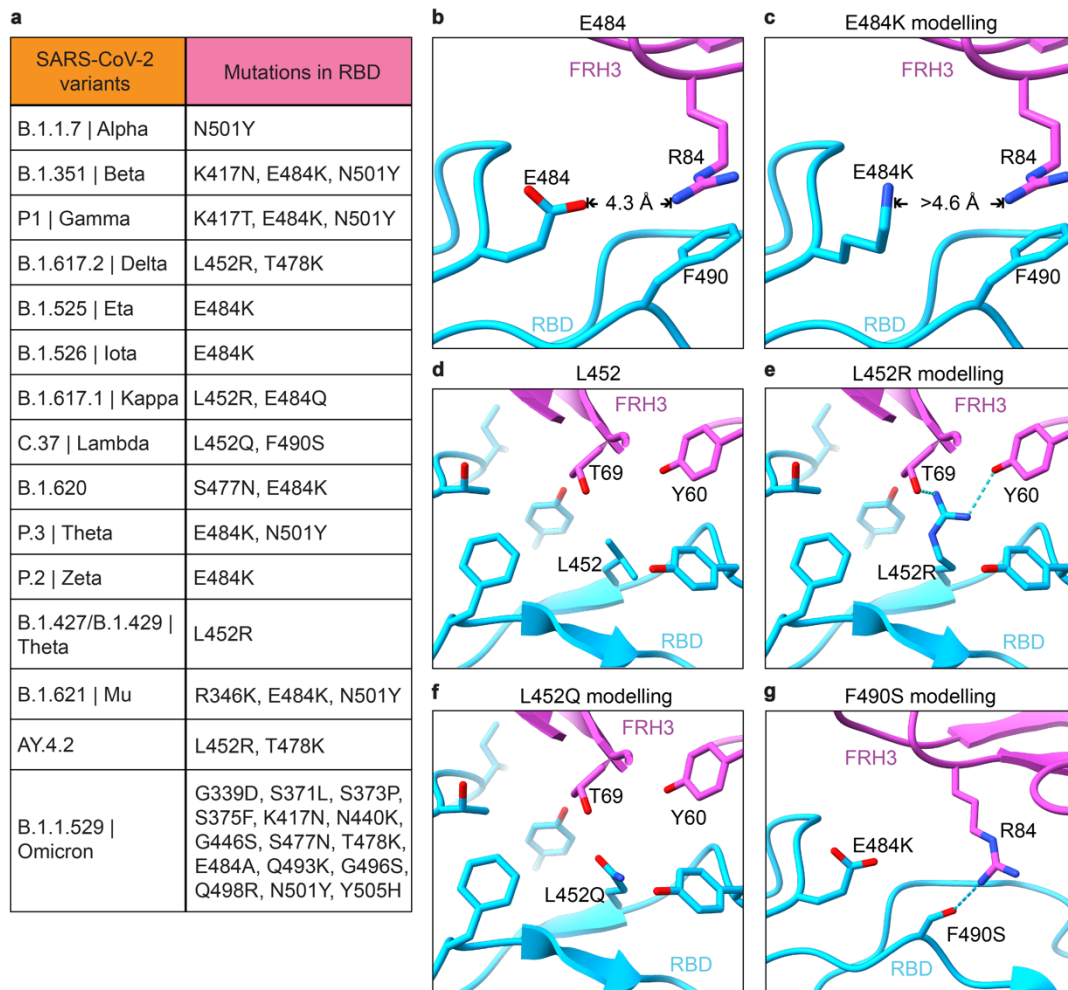
933 **Figure 4**



934
935

936 **Fig. 4 Structural basis and neutralizing mechanism for the broad neutralizing**
937 **activities of 35B5 to the SARS-CoV-2 variants. a** Structural comparisons of the
938 35B5 Fab-“up” RBD interactions with those of the previously identified Class 2 and 3
939 neutralizing antibodies. 35B5 Fab and the Fab regions of the representative antibodies
940 CV07-270 and REGN10987 from Class 2 and 3, respectively, are illustrated in
941 cartoon and colored as indicated. RBD is represented as surface in yellow. **b**
942 Comparison of the epitope of 35B5 with those of the representative neutralizing
943 antibodies of Class 2 and 3 on RBD. The 35B5 epitope is colored in cyan. The
944 epitopes of CV07-270 (Class 2) and REGN10987 (Class 3) are labeled using red and
945 black lines, respectively. **c** Mapping of the frequently mutated residues of the spike
946 protein in the recent SARS-CoV-2 variant in the 35B5 Fab-RBD structure. RBD and
947 35B5 Fab are shown in cartoon and colored in yellow and purple, respectively. The
948 frequently mutated residues in RBD in the recent SARS-CoV-2 variant are
949 highlighted with green spheres. **d** Interactions of 35B5 Fab with the “down” RBD.
950 35B5 Fab, the “down” RBD and NTD domains are colored in purple, cyan and grey,
951 respectively. The 35B5 Fab-interacting region on RBD is highlighted in orange. **e**
952 Structural clashes between 35B5 Fab and the NTD domain upon structural
953 superimposition of the “up” RBD-35B5 Fab model with the “down” RBD-35B5 Fab
954 region in the state 1 S-6P-35B5 Fab complex. The structural clashes are highlighted
955 with dashed lines. **f** Conformational changes of the RBD domains upon 35B5 Fab
956 binding. The S-6P-35B5 Fab complex structures of three states were superimposed.
957 35B5 Fabs are shown in cartoon in purple. The “down”, “up”, and “releasing” RBD
958 domains are colored in blue, yellow and red, respectively. The conformational
959 changes of RBDs are indicated with arrows. **g** Schematic diagram of the neutralizing
960 mechanism of 35B5 against SARS-CoV-2. The “down” and “up” RBDs in the
961 tight-closed or loose-closed S trimers are colored in blue and yellow, respectively.
962 The conformation changes and transmission of RBDs from the “down” to “up”,
963 finally to “releasing” states are shown as red arrows.

964 **Figure 5**



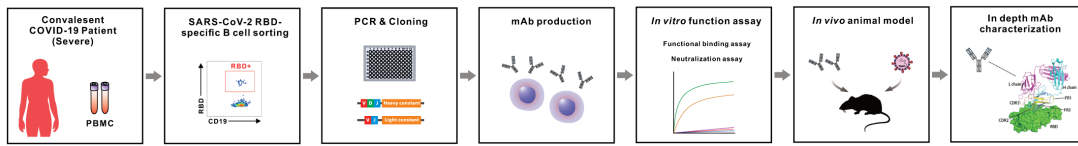
965

966

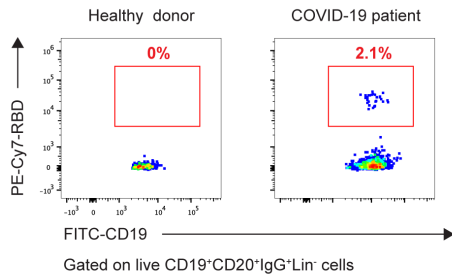
967 **Fig. 5 Interactions of 35B5 Fab with RBD.** **a** Mutations in the RBD of reported
968 SARS-CoV-2 variants of concern or interest. **b-g** The residues E484 (**b**) and L452 (**d**)
969 are not involved in the interactions of RBD with 35B5 Fab. E484 is more than 4.2 Å
970 away from 35B5 R84, which forms cation- π interaction with RBD F490. The E484K
971 mutation in RBD does not interact with 35B5 R84 through molecular modelling (**c**).
972 The L452Q modelling suggests none interactions formed at this site with 35B5 (**f**). In
973 structural modeling, the L452R mutation (**e**) and F490S mutation (**g**) in RBD
974 generates potential additional interactions with 35B5 Fab. Potential hydrogen bonds
975 are shown as dashed lines.

Supplementary Figure 1

a



b



c

CDR3 sequence of 35B5 mAb heavy chain

A K A V E M V R G L M G L G A D P E Y G M D V

CDR3 sequence of 35B5 mAb light chain

M Q A L Q T P F T

d

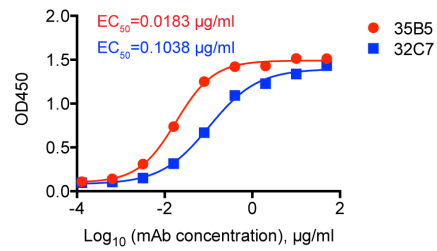
CDR3 sequence of 32C7 mAb heavy chain

A R D T E D C S S T T C Y V D Y

CDR3 sequence of 32C7 mAb light chain

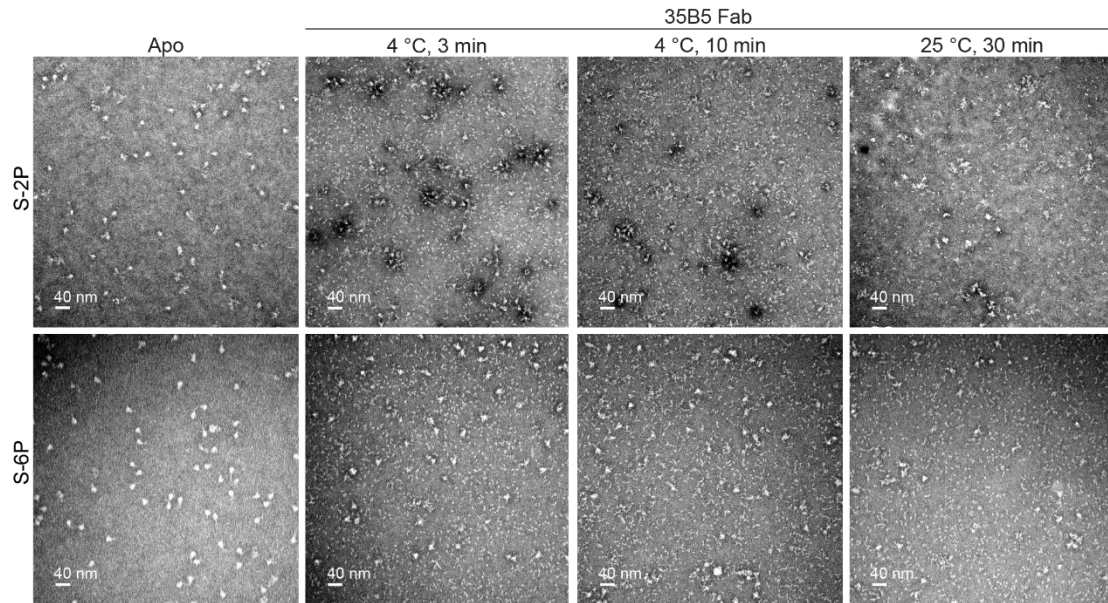
H Q Y Y S T P F T

e



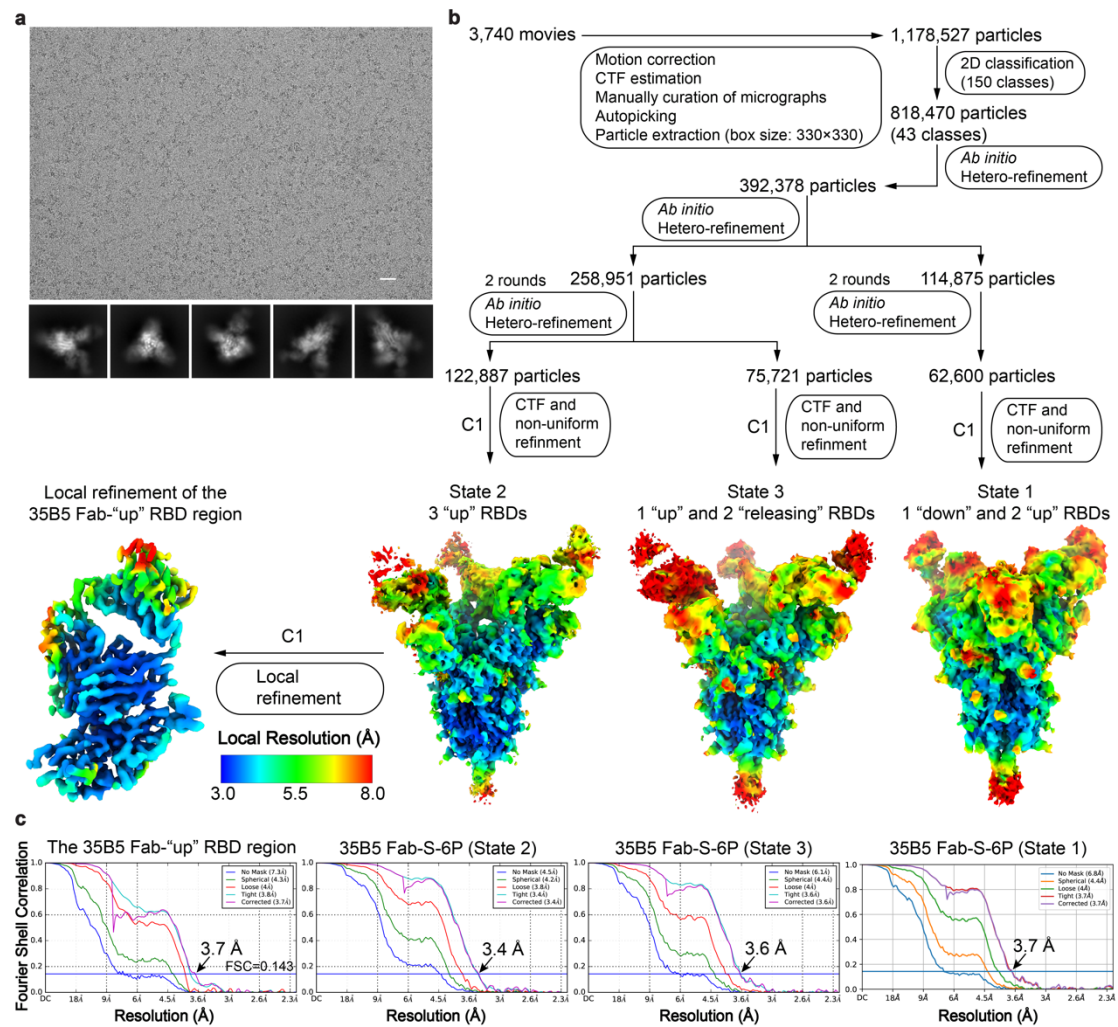
Supplementary Figure 1. Isolation of potent SARS-CoV-2 neutralizing mAbs from COVID-19 convalescent patients. **a** Isolation strategy of SARS-CoV-2 neutralizing mAbs. **b** Flow cytometry analysis of SARS-CoV-2 RBD-specific B cells from the PBMC of healthy donors and COVID-19 convalescent patients. The numbers adjacent to the outlined area indicate the proportions of SARS-CoV-2 RBD-specific B cells in CD19⁺CD20⁺IgG⁺ B cells. **c, d** The CDR3 sequences of mAb 35B5 (**c**) and mAb 32C7 (**d**). **e** ELISA analysis of mAb 35B5 (red) or mAb 32C7 (blue) binding to SARS-CoV-2 RBD protein. EC₅₀, concentration for 50% of maximal effect.

Supplementary Figure 2



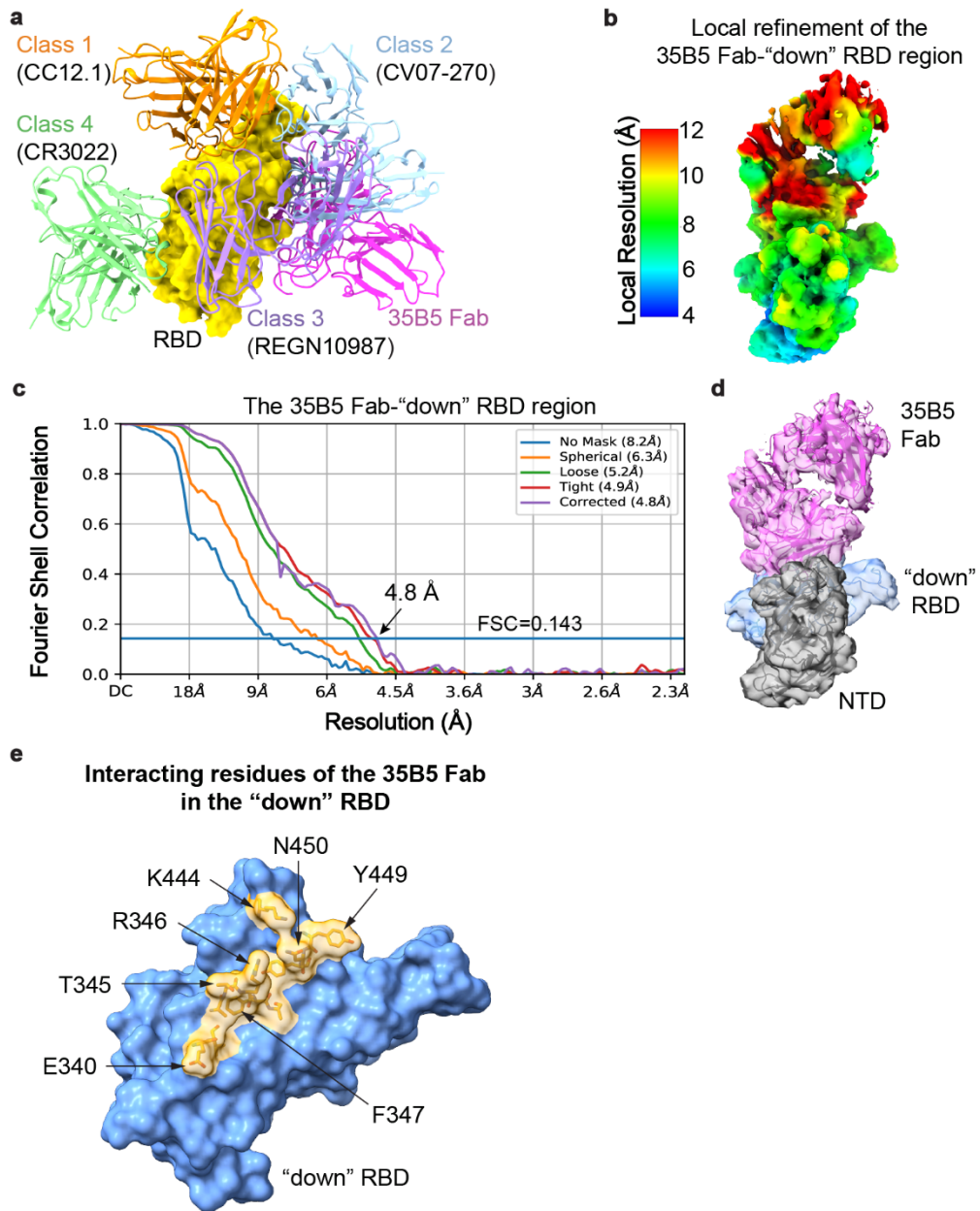
Supplementary Fig. 2 Representative negative-staining EM micrographs of the S-2P and S-6P trimers after the treatment of 35B5 Fab. The S-2P and S-6P trimeric proteins were treated with or without 35B5 Fab for indicated time at 4°C or 25°C before negative staining analysis. Scale bar, 40 nm.

Supplementary Figure 3



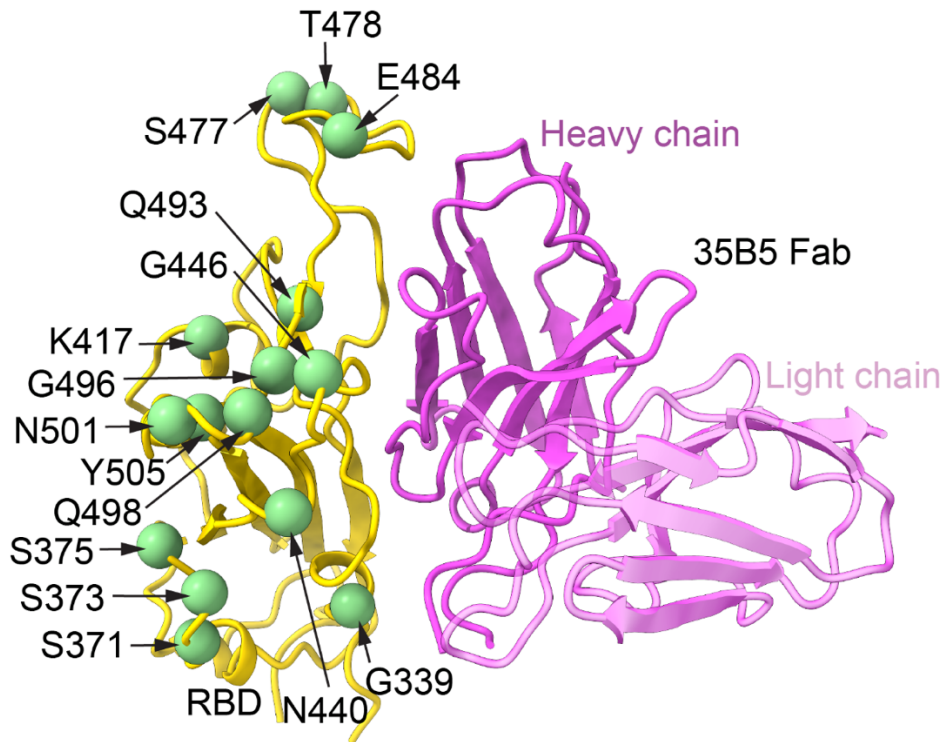
Supplementary Fig. 3 Cryo-EM data processing and validation of the S-6P-35B5 Fab complex. **a** Representative cryo-electron micrograph (upper) and 2D class averages (lower) of the S-6P-35B5 Fab complex. Scale bar, 25 nm. **b** Cryo-EM data processing flow-chart of the S-6P-35B5 Fab complex. Three states of the S-6P-35B5 Fab complex were obtained in data collection. Local refinement of the 35B5Fab-“up” RBD region was carried out using C1 symmetry (left). All density maps were prepared using ChimeraX. The map resolution is color coded for different regions. The resolution goes from 2.8 to 6.0 Å. **c** The Fourier shell correlation (FSC) curves for the reconstructions in **b**. The resolution estimations of cryo-EM density maps were based on the corrected FSC curves at the gold standard FSC=0.143 criterion.

Supplementary Figure 4



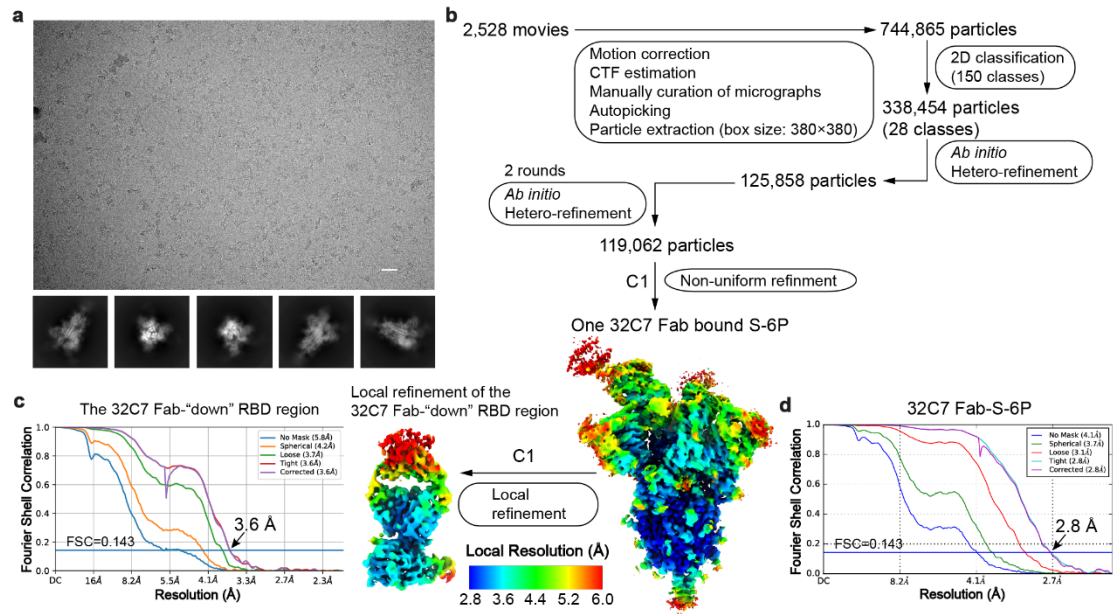
Supplementary Fig. 4 Comparison of 35B5 with other mAbs and the local refinement of 35B5 Fab-“down” RBD region. **a** Structural comparisons of the 35B5 Fab-“up” RBD interactions with those of the previously identified four classes of neutralizing antibodies. 35B5 Fab and the Fab regions of the representative antibodies CC12.1, CV07-270, REGN10987 and CR3022 from Class 1-4, respectively, are illustrated in cartoon and colored as indicated. RBD is represented as surface in yellow. **b** Local refinement of the region of 35B5 Fab with the “down” RBD and NTD domains in the State 1 S-6P-35B5 Fab complex. The density map was prepared using ChimeraX. The map resolution is color coded for different regions. The resolution goes from 4.0 Å to 12 Å. **c** The Fourier shell correlation (FSC) curve for the reconstructions in **b**. The resolution estimation (4.8 Å) of cryo-EM density maps were based on the corrected FSC curves at the gold standard FSC=0.143 criterion. **d** Structural modeling of 35B5 Fab with the “down” RBD and NTD domains in the density map obtained from the local refinement in **b**. 35B5 Fab, RBD and NTD are colored in purple, blue and grey respectively. **e** The 35B5-interacting residues of the “down” RBD. The 35B5-interacting residues of the “down” RBD (within 4 Å to 35B5 Fab) are colored in yellow.

Supplementary Figure 5



Supplementary Fig. 5 Structural mapping of RBD mutations in SARS-CoV-2 omicron variant onto the 35B5 Fab-RBD structure. Mapping of the mutated residues of the spike protein in SARS-CoV-2 omicron variant onto the 35B5 Fab-RBD structure. RBD and 35B5 Fab are shown in cartoon and colored in yellow and purple, respectively. The mutated residues in RBD in SARS-CoV-2 omicron variant are highlighted with green spheres.

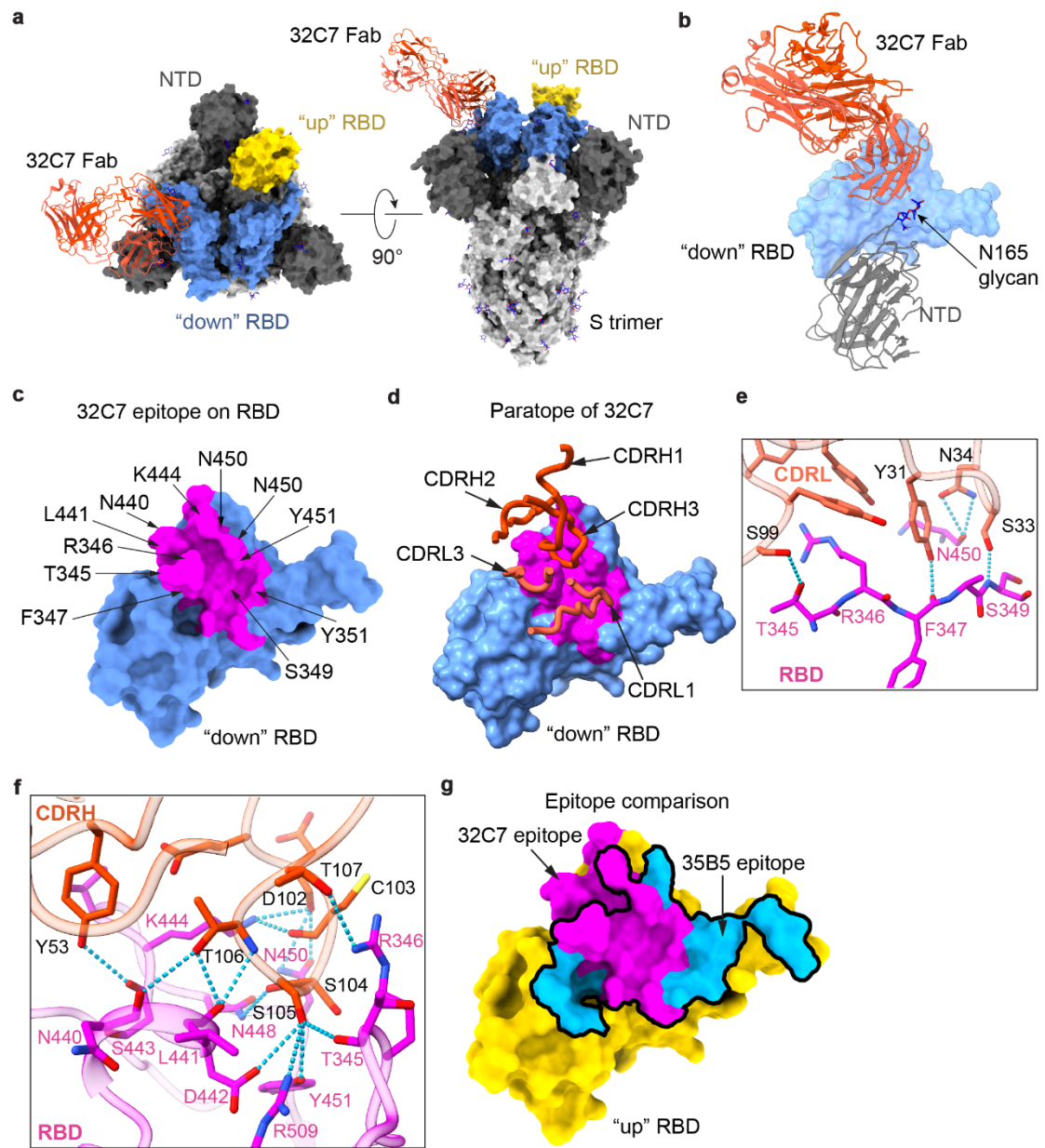
Supplementary Figure 6



Supplementary Fig. 6 Cryo-EM data processing and validation of the S-6P-32C7

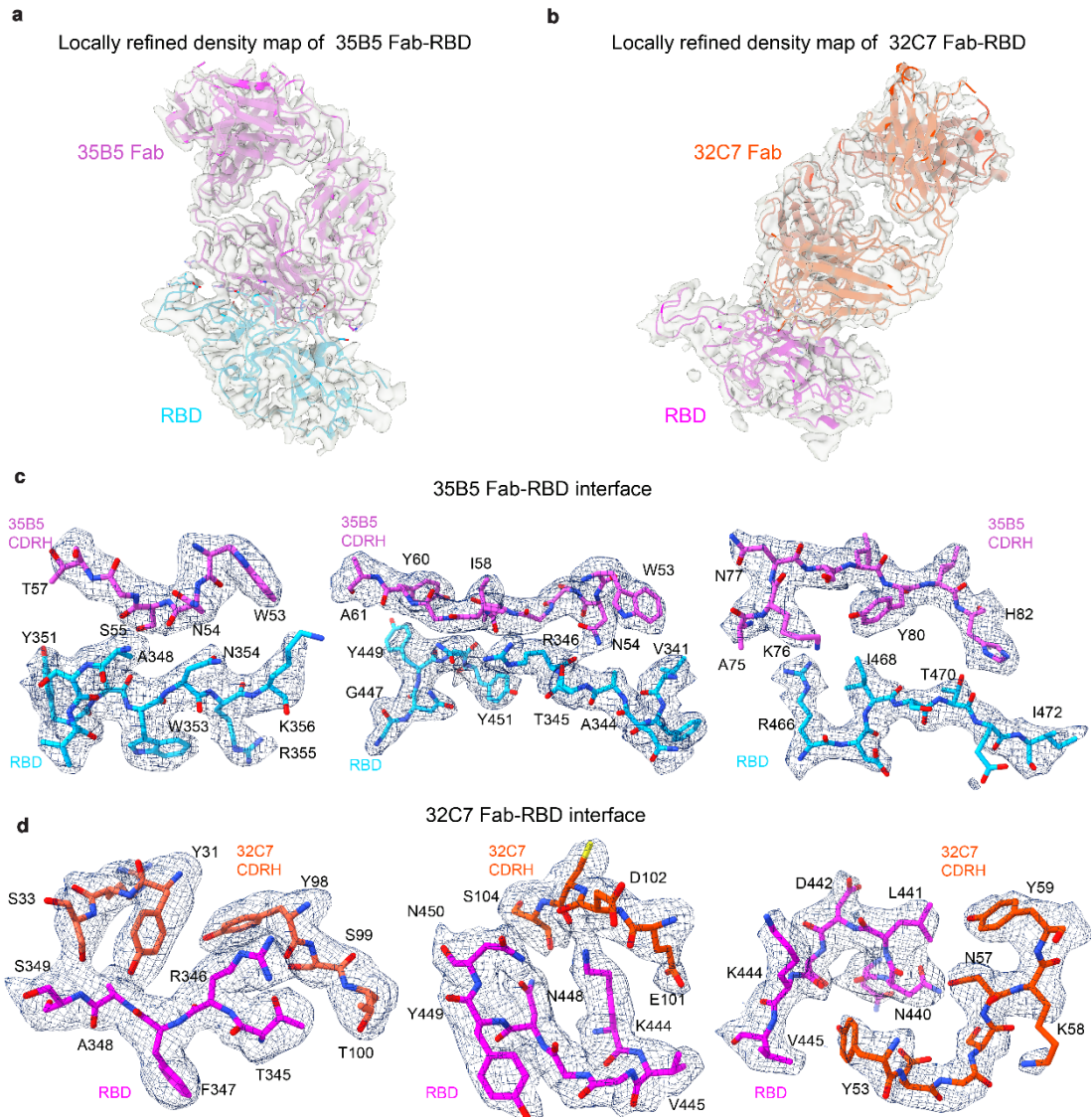
Fab complex. a Representative electron micrograph (upper) and 2D class averages (lower) of the SARS-CoV-2 S-6P- 32C7 Fab complex. Scale bar, 25 nm. **b** The cryo-EM data processing flow chart of the S-6P-32C7 Fab complex. Only one 32C7 Fab is bound to a “down” RBD of the S-6P trimer. Local refinement of 32C7 Fab with the “down” RBD generated a map at the resolution of ~ 3.6 Å. The density map was prepared using ChimeraX. The map resolution is color coded for different regions. The resolution goes from 2.8 Å to 6.0 Å. **c, d** The FSC curves for the reconstructions of the 32C7 Fab-RBD region (**c**) and the S-6P-32C7 Fab complex (**d**) in **b**. The resolution estimations of cryo-EM density maps were based on the corrected FSC curves at the gold standard FSC=0.143 criterion.

Supplementary Figure 7



Supplementary Fig. 7 Cryo-EM structure of the S-6P-32C7 Fab complex. **a** The 2.8-Å cryo-EM structure of the S-6P-32C7 Fab complex. The S-6P trimer is represented as surface. 32C7 Fab is shown in cartoon in red. The “down” and “up” RBDs are colored in blue and yellow, respectively. **b** Structural superposition of the 32C7 Fab-RBD model and the tight-closed S trimer (PDBID: 6ZB5). In the structural superimposition, 32C7 Fab does not form structural clashes with the NTD domain of the tight-closed S trimer. RBD is shown as surface in blue. The NTD domain of the S trimer is shown in cartoon in grey. **c** The 32C7 epitope on RBD. The epitope residues are labeled as indicated. **d** The RBD-interacting regions in 32C7 Fab. The CDRH1, CDRH2, CDRH3, CDRL1 and CDRL3 are shown in ribbon. **e, f** Detailed interactions of the light chain CDRs (**e**) and heavy chain CDRs (**f**) of 32C7 Fab with RBD. Hydrogen-bond interactions are shown as dashed lines. **g** Comparison of the epitopes for 32C7 and 35B5 on the surface of RBD. The epitopes for 32C7 and 35B5 (black contour) are colored in purple and blue, respectively.

Supplementary Figure 8



Supplementary Fig. 8 Density maps of 35B5 Fab-RBD and 32C7 Fab-RBD interfaces after local refinement. **a** Locally refined density map (transparent gray) of the 35B5 Fab-“up” RBD region in the State 2 S-6P-35B5 Fab complex. **b** Locally refined density map of the 32C7 Fab-RBD region in the S-6P-32C7 Fab complex. **c** Representative density maps of interaction regions at the 35B5 Fab-RBD interface. **d** Representative density maps of interaction regions at 32C7 Fab-RBD interface. The interacting residues of RBD and Fabs are shown as stick.

Supplementary Table 1. Cryo-EM data collection and refinement statistics.

	35B5 Fab-S-6P (state 1)	35B5 Fab-S-6P (state 1, local refinement)	35B5 Fab-S-6P (state 2)	35B5 Fab-S-6P (state 2, local refinement)	35B5 Fab-S-6P (state 3)	32C7 Fab-S-6P	32C7 Fab-S-6P (local refinement)
PDB code	7E9N	7F46	7E9O	7E9P	7E9Q	7ENF	7ENG
EMDB code	EMD-31033	EMD-31444	EMD-31034	EMD-31035	EMD-31036	EMD-31209	EMD-31210
Data collection and processing							
Voltage (kV)	300	300	300	300	300	300	300
Magnification	81,000	81,000	81,000	81,000	81,000	81,000	81,000
Pixel size (Å/pix)	0.5475	0.5475	0.5475	0.5475	0.5475	0.53865	0.53865
Frames per exposure	32	32	32	32	32	32	32
Exposure (e ⁻ /Å ²)	50	50	50	50	50	50	50
Defocus range (µm)	1.2 to 1.3	1.2 to 1.3	1.2 to 1.3	1.2 to 1.3	1.2 to 1.3	1.4 to 1.8	1.4 to 1.8
Final particle images (no.)	62,600	62,600	122,887	122,886	75,721	119,062	119,062
Symmetry imposed	C1	C1	C1	C1	C1	C1	C1
Map resolution (Å, 0.143 FSC threshold)	3.7	4.8	3.4	3.7	3.6	2.8	3.6
Refinement							
Map resolution (Å, 0.5 FSC threshold)	3.9	8.6	3.7	3.9	3.8	3.0	3.7
Map sharpening <i>B</i> factor (Å ²)	81.9	115.6	90.4	86.3	82.5	75.8	110.2
Model composition							
Protein residues	4,313	842	4338	639	4,338	3,390	640
Ligands	27	2	27	1	27	53	2
R.m.s. deviations							
Bond length (Å)	0.008	0.005	0.004	0.005	0.005	0.005	0.006
Bond angles (°)	0.870	0.757	0.768	0.849	0.887	0.835	0.802
Ramachandran plot							
Favored (%)	91.61	91.12	95.12	92.53	93.60	94.70	92.59
Allowed (%)	8.39	8.88	4.88	7.47	6.40	5.30	7.41
Outliers (%)	0	0	0	0	0	0	0
Validation							
Poor rotamers (%)	0.11	0	0.24	0	0.32	0.56	0.36
Clash score	12.95	18.16	10.62	11.97	14.62	10.14	14.32
MolProbity score	2.12	2.27	1.88	2.06	2.09	1.89	2.13